Temporally constant Quaternary uplift rates and their relationship with extensional upper-plate faults in south Crete (Greece), constrained with ^{36}Cl cosmogenic exposure dating.

J. Robertson[1*], M. Meschis[1], G.P. Roberts[1], A. Ganas[2], D. Gheorghiu[3]

[1]Department of Earth and Planetary Sciences, Birkbeck College, University of London, WC1E 7HX, UK.

[2] Institute of Geodynamics, National Observatory of Athens, 11810 Athens, Greece

[3] Scottish Universities Environmental Research Centre, UK

Corresponding author: Jenni Robertson (j.robertson@praxisuk.co.uk)

Key points:

- **Uplift rates in S. Crete vary spatially as a result of upper-plate faulting**
- **Uplift rates appear to have been temporally constant for up to 600 - 900 ka**
- **The South Central Crete Fault is an active fault with a throw rate of 0.41 mm/yr**

Abstract

Preserved sets of marine terraces and palaeoshorelines above subduction zones provide an opportunity to explore the long-term deformation that occurs as a result of upper-plate extension. We investigate uplifted palaeoshorelines along the South Central Crete Fault (SCCF) and over its western tip, located above the Hellenic Subduction Zone, in order to derive uplift rates and examine the role that known extensional faults contribute to observed coastal uplift. We have mapped palaeoshorelines and successfully dated four Late-Quaternary wave-cut platforms using *in-situ* ^{36}Cl exposure dating. These absolute ages are used to guide a correlation of palaeoshorelines with Quaternary sea-level highstands from 76.5 to ~900 ka; the results of which suggest that uplift rates vary along fault strikes but have been constant for up to 600 ka in places. Correlation of palaeoshorelines across the SCCF results in a throw-rate of 0.41 mm/yr and, assuming repetition of 1.1 m slip events, a fault-specific earthquake recurrence interval of approximately 2700 years. Elastic-half space modelling implies that coastal uplift is related to offshore upper-plate extensional faults. These faults may be responsible for perturbing the uplift rate signals in the south central Crete area. Our findings suggest that where uplifted marine terraces are used to make inferences about the mechanisms responsible for uplift throughout the Hellenic Subduction Zone, and other subduction zones worldwide, the impact of upper-plate extensional faults over multiple seismic cycles should also be considered.

1. Introduction

Crete is situated above the Hellenic subduction zone (HSZ) and has been used to study the relationship between uplift and slip associated with the HSZ (Gallen et al., 2014; Papadimitriou & Karakostas, 2008; Shaw et al., 2008; Shaw & Jackson, 2010; Strobl et al., 2014). Observations from uplifted palaeoshorelines (e.g Gallen et al., 2014; (Mouslopolou et al., 2015a; Mouslopolou et al., 2015b; Pirazzoli et al., 1982; Shaw et al., 2008; Tsimi et al., 2007), Palaeolithic sites (Strasser et al., 2011), alluvial fans (Mouslopolou et al., 2017; Pope et al., 2008) and other geomorphological and biological features (Kelletat, 1991; Shaw et al., 2010) along its south and west coasts have been used to discuss the relationships between slip on the subduction interface, thrust faults in the overlying wedge, and historic tsunamigenic earthquakes (Ganas & Parsons, 2009; Shaw et al., 2008; Shaw & Jackson, 2010; Stiros, 2010). However, less attention has been given to the role of active normal faulting in influencing uplift, a phenomenon that is widespread on Crete (Angelier, 1979a; Armijo et al., 1992; Caputo et al., 2010; Gallen et al., 2014; Ganas et al., 2017). The upper-plates of subduction zones throughout the World have been shown to host onshore and offshore upper-crustal normal faults (e.g: Binnie et al., 2016; Bottner et al., 2018; Cashman and Kelsey, 1990; Howell et al., 2016; McIntosh et al., 1993; McNeill et al., 1998; Meschis et al., 2018; Monaco and Tortorici, 2001; Papanikolaou et al., 2007; Wessel et al., 1994). Where extensional faults occur near to the coastline they leave clear geomorphic signatures of the often variable deformation they cause (Armijo et al., 1996; Meschis et al., 2018; Papanikolaou et al., 2007; Roberts et al., 2009; Roberts et al., 2013) as a result of differential uplift or subsidence between the centre (maximum displacement) and tips (minimum displacement) of the faults. It follows, therefore, that onshore and offshore extensional faults in the upper plate of subduction zones may have the capacity to influence coastal uplift and that uplift rates inferred using coastline data represent a combination of mechanisms including upper-plate extensional faulting (McNeill et al.,1998).

In order to understand the relationships between coastal uplift and the broader tectonic influences that occur within a subduction zone setting it is important to consider the impact of upper-plate extensional faults. If we can quantify the deformation that occurs on the length scale of a number of normal faults along the southern Crete coastline, this may, in the future, allow us to explore the component of uplift caused by subduction-related activities that tend to occur on far longer length scales (e.g. Ozawa et al., 2011; Subarya et al., 2006; Vigny et al., 2011). This, in turn, would lead to detailed analysis of the independent seismic hazard posed by normal faults in addition to the hazard related to the converging plate boundary.

While normal faults in many parts of Crete are known to be active in the Holocene (Armijo et al., 1992; Caputo et al., 2006; Caputo et al., 2010; Ganas et al., 2017; Monaco & Tortorici, 2004), the longer term activity through the Quaternary is less well-known, in part due to the lack of absolute age control on the Quaternary geology and geomorphology. Inferring the time-averaged uplift behaviour linked to the HSZ and upper-plate deformation over multiple seismic cycles requires robust dating techniques which extend into the Late Quaternary. Presently, there are few sets of existing dates from the south central area of Crete. Determining long-term uplift rates also allows us to explore how these compare to shorter timescales.

We investigate a key location along the south central coast of Crete, where a normal fault (South Central Crete Fault – SCCF) crosses the coastline, producing differential uplift, with Quaternary marine terrace deposits at elevations that vary along the coast. To the west where the SCCF crosses the coast at Tsoutsourous Bay (TB) (Figures 1 and 2), palaeoshorelines are cut into a steep, high relief coastal area with greater vertical spacing between them in comparison to those to the east of TB where the palaeoshorelines are more closely spaced together and cut into a low relief coastal plain. Owing to the variation in geology, relief, and elevation of Quaternary palaeoshorelines, and the fact that the SCCF has a clear Holocene scarp with dramatic fault planes exposed near Arvi, we think it is an active fault, capable of hosting destructive earthquakes.

The application of a new dating approach allows important new insights. The preservation of geomorphological features associated with wave-cut platforms provides evidence of minimal erosion, thus facilitating the use of *in-situ* ^{36}Cl cosmogenic exposure dating. We have obtained ^{36}Cl exposure ages from five wave-cut platform sites, providing dates for palaeoshorelines that would not be amenable to conventional Optically Stimulated Luminescence (OSL) sediment dating or Uranium-series coral dating. These new ^{36}Cl exposure ages alongside synchronous correlation modelling using sea-level curve data provide new insights that allow us to explore how uplift rates change spatially and temporally. Elastic-half space modelling allows us to compare the observed and modelled patterns of uplift rates in order to establish the significance that extensional upper-plate faults have with regard to coastal uplift. Finally, we discuss the implications of our findings within the context of seismic hazard, and local and broader tectonic regimes of the HSZ and suggest that as coastal uplift along the south of Crete appears to be dominated by extensional faulting this may also be true of the rest of the HSZ.

.

2. Background

The Hellenic subduction zone (HSZ) is over 1200 km long and is one of the most seismically active regions on Earth (Becker & Meier, 2010). It accommodates convergence between the Eurasian and African plates at a rate of ~35-40 mm/yr (Nocquet, 2012) (Figure 1), with much of this convergence occurring as a result of the southward motion of the Eurasian plate (Jackson, 1994). Crete lies in the forearc of the HSZ, a number of authors suggest that Crete represents a horst structure that has been uplifting since the Miocene (Bohnhoff et al., 2001; Meier et al., 2007; Papanikolaou & Vassilakis, 2010; Ten Veen and Meijer., 1998) but this is not widely accepted (Caputo et al., 2010; Meulenkamp et al., 1994; van Hinsbergen and Meulenkamp, 2006)

2.1 *Crete geology and tectonics*

The variation of lithologies observed on Crete exists predominantly as a result of deformation that has occurred throughout the Oligocene to the early Miocene in the form of south-directed thrusting (Fassoulas et al., 1994, and references therein; Papanikolaou & Vassilakis, 2010). The result of this compression was stacking of the internal and external nappe zones (IGME map sheets Ano Viannos 1:50,000; IGME Akhendhrias 1:50,000). The south-central Crete area is bounded by two mountain ranges: the Asterousia mountains in the west and the Dikti mountains in the east (Figure 1c). The hangingwall of the SCCF, which is bounded by the Dikti mountain range to the north, is predominantly comprised of middle-upper Miocene sediments juxtaposed with ophiolitic and flysch deposits from the internal and external zones nappes (IGME Ano Viannos 1:50,000). To the west, beyond the western tip of the SCCF, the lithology is dominated by limestones of variable age (Mesozoic to Tertiary), and their unconsolidated and consolidated scree deposits that make up the Asterousia mountain range (IGME map sheet Akhendhrias 1:50,000). Marine terrace deposits are reported throughout the area and are seen as conglomeratic beach rocks, gravels and sands which unconformably overlie eroded Miocene sediments and limestone surfaces (Gallen et al., 2014). Quaternary and Holocene alluvial fan deposits are common throughout the study area, especially along the hangingwall of the SCCF (Gallen et al., 2014). Associated with the marine terrace deposits are (a) palaeoshorelines, located up-dip from the terrace deposits, defined by palaeo- sea-cliffs cut into bedrock limestones, marked by shoreline notches lined with lithophagid borings and other shoreline fauna (algal encrustations, gastropods, echinoderms, bivalves and, rarely, corals), and (b) wave-cut platforms, that are the along strike correlatable surfaces to marine terrace deposits, characterised by erosive surfaces marked with millholes that are in turn marked by lithophagid borings. The borings are between 3-9 cm deep when formed (Peharda et al., 2015), though research by Devescovi and Ivesa, (2008) suggest a value closer to 6 cm is common, so their preservation with depths of a few centimetres indicates minimal erosion since their formation.

2.1.1 *Upper plate faults and their context within a converging zone*

While thrust faulting dominates the offshore of southern Crete at depths above and along the subduction interface, shallower depths of <15 km and closer to the southern shoreline of Crete are predominantly characterized by normal and transtensional faulting

(Alves et al., 2007; Kokinou et al., 2012; Papazachos, 1990; Ten Veen and Kleinspehn., 2003). Onshore, normal faulting is prevalent, with the strikes of these dip-slip faults having multiple directions suggesting a complex extensional regime (Caputo et al., 2010; Ganas et al., 2017; Mercier et al., 1987; Zygouri et al., 2016). The active normal faults broadly trend E-W or N-S with the exception of the Ierapetra and Kastelli faults which trend NE-SW (Strobl et al., 2014) (Figure 1a). The E-W trending faults that accommodate arc-perpendicular extension are common, both onshore and offshore of south Crete; these faults are the subject of this study.

Onshore E-W trending normal faults show uplift in their footwalls, as expected, but also uplift in their hangingwalls, indicated by preserved marine terraces, despite the subsidence they are experiencing as a result of faulting. The hangingwall subsidence is counteracted by uplift, presumably related to the subduction interface and/or thrust faults in the overlying wedge and/or footwall uplift from offshore, E-W striking normal faults. Uplift in the hangingwall of normal faults is observed along the south coast of Crete, namely the Sfakia fault, SW Crete (Skourtsos et al., 2007, Tsimi et al., 2007), the Ierapetra fault, SE Crete (Gaki-Papanastassiou et al., 2009) and the SCCF (Angelier, 1979b; Gallen et al., 2014; Gallen & Wegmann, 2016).

We are interested in the onshore SCCF along the southern central area of Crete (Figure 1a), because it crosses the coast and appears to control differential uplift that can be explored through mapping and dating of wave-cut platforms. Limestone fault scarps are visible along all four of its south-dipping segments and have an average dip of 45^{o} (Gallen et al., 2014). Converging slip vectors reported along its ~45 km onshore length (Gallen et al., 2014) suggest that the segments represent one fault at depth (Michetti et al., 2000; Roberts & Ganas, 2000; Roberts, 1996, 2007). The western section of the SCCF fault exhibits a change in strike as it curves toward the coastline and tips-out offshore (Figures 2, 3). Analysis of bathymetry defines the approximate offshore extent of this fault as ~2.5 km south of the coastline (Figure 3a) (Alves et al., 2014; Kokinou et al., 2012). This interpretation contrasts with the suggestion by Gallen and Wegmann, (2016) where the SCCF represents the onshore extension of the Ptolemy fault, which they suggest has a normal motion, implying in an intra-plate normal fault which is ~124 km in length. This length is at odds with the notion that maximum fault length is about twice the depth of the seismogenic layer of 12-15 km (Jackson & White, 1989), so we prefer our interpretation which defines a ~45 km fault.

Offshore, the southern coast of Crete is bounded by active normal faults and three 'trench' faults. The normal faults, the Cape Lithino faults and the Mirto fault (Caputo et al., 2010) (Figure 1a), have a dip to the south, synthetic to the SCCF. Investigations using bathymetry, seismic reflection and sediment core data by Alves et al. (2007) and Kokinou et al. (2012) showed that the faults are active and control basin development. The Ptolemy, Pliny and Strabo 'trenches' are upper-plate faults that do not represent the subduction trench of Crete, which is buried under up to 10 km of sediments belonging to the accretionary prism (Chaumillon & Mascle, 1997).

The Ptolemy fault trends NE to NNE (Angelier et al., 1982) and extends ~90 km along strike (Figure 1). The motion on this fault has been the subject of much debate with earlier studies suggesting that it either accommodates convergence as a transform/thrust fault (Mascle et al., 1982; McKenzie et al., 1978; Taymaz et al., 1990), is a strike-slip fault (Chaumillion & Mascle, 1997; Huguen et al., 2001; Pichon & Angelier, 1979) or is a normal fault (Gallen et al., 2014; Gallen & Wegmann, 2016). However, evidence from microseismicity, bathymetry, seismic reflection and analysis of fault-plane solutions suggest that the active fault cuts through the entire upper plate, is south dipping, near vertical (85^{o}) and records sinistral transtensional motion that has resulted in the development of a wedgeshaped sedimentary basin approximately 4 km thick (Becker et al., 2006; Bohnoff et al., 2001; Kokinou et al., 2012; Meier et al., 2004).

2.2 *Crete uplift*

The cause of uplift on Crete is debated and suggested to result from underplating on the subduction interface, reverse motion on the megathrust, thrusting and oblique slip faulting in the forearc, and active normal faulting (Angelier et al., 1982; Caputo et al., 2010; Gallen et al., 2014; Ganas & Parsons, 2009; Meier et al., 2007; Mouslopoulou et al., 2015a; Shaw et al., 2008; Strobl et al., 2014; Taymaz et al., 1990; Tiberti et al., 2014). Geodetic, seismological and geological evidence suggest compressional, extensional and strike-slip tectonics onshore and offshore southern Crete as seen by the analysis of fault plane solutions and microseismicity studies (Becker et al., 2010; Bohnhoff et al. 2005; Caputo et al., 2010; Doutsos & Kokkalas, 2001; Howell et al., 2017; Kokinou et al., 2012; Meier et al., 2007; Papazachos, 1990; Shaw & Jackson, 2010; Taymaz et al., 1990). These studies show that thrust faulting occurs as a result of forearc-normal compression at depths linked to subduction to the south of Crete; additionally Shaw et al. (2008) suggested that reverse (high-angle) splay faults may cut the upper crust in western Crete, however their existence was debated by Ganas and Parsons, (2009) on the basis of lack of compatible seismological data. The E-W and N-S trending normal faults accommodate arc-normal and arc-parallel extension (Angelier, 1979a; Armijo et al., 1992; Caputo et al., 2006; Caputo et al., 2010; Fassoulas., 2000; Floyd et al., 2010; Gallen et al., 2014; Gallen & Wegmann, 2016; Ganas et al., 2017; Howell et al., 2017; Kokinou et al., 2012; Peterek & Schwarze, 2004; Snopek et al., 2007), which is also reflected in Eurasian (upper) plate GPS motions that increase toward the southern edge of the plate in the location of Crete (Floyd et al., 2010; McClusky et al., 2000) and are quantified by Nocquet et al., 2012 as ~10 mm/yr.

Pleistocene uplift is visible in sequences of preserved marine terraces seen throughout the eastern and southern coasts of Crete (Angelier, 1979b; Gaki-Papanastassiou et al., 2009; Gallen et al., 2014; Peterek & Schwarze, 2004; Pirazzoli et al., 1982; Strobl et al., 2014). Uplift continues into the present day, evidenced by raised Holocene notches and raised beach deposits which are predominantly seen in Western Crete and linked to suggested coseismic uplift caused by the 365 A.D. earthquake (Pirazzoli et al., 1982; Postma & Nemec, 1990; Shaw et al., 2008; Stiros, 2001, 2010). Uplifted Holocene beachrocks are also reported on the footwall of the Ierapetra fault toward the south east of the island (Figure 1c; see Gaki-Papanastassiou et al., 2009 and references therein).

Investigations using uplifted hangingwall and footwall marine terraces, 2D viscoelastic modelling and sedimentary correlations have led to a large variety of uplift estimates along the south coast of Crete from 0.2 - 7.7 mm/yr over timescales since the late Quaternary (~600 ka) to the present day (Gaki-Papanastassiou et al., 2009; Gallen et al., 2014; Gallen & Wegmann, 2016; Meulenkamp et al., 1994; Mouslopoulou et al., 2017; Mouslopoulou et al., 2015a; Mouslopoulou et al., 2015b; Shaw et al., 2008; Skourtsos et al., 2007; Strasser et al., 2011; Strobl et al., 2014; Tiberti et al., 2014). Additionally, some authors propose that uplift rates have significantly varied over time (Gallen et al., 2014; Mouslopoulou et al., 2015a; Tiberti et al., 2014). Studies to determine uplift rates have employed a mixture of dating techniques with many attempting to explore long-term uplift using AMS ^{14}C radiocarbon dating on marine shells (Mouslopoulou et al., 2015b; Mouslopoulou et al., 2015a; Shaw et al., 2008; Shaw et al., 2010; Shaw, 2012; Strasser et al., 2011; Tiberti et al., 2014) which has a maximum dating span of around ~50 ka (Reimer et al., 2013); other methods include ^{10}Be exposure dating (Strobl et al., 2014), Optically Stimulated Luminescence (OSL) geochronology (Gallen et al., 2014) and U-Series measurements (Angelier 1975b; Gaki-Papanastassiou et al., 2009).

The pattern of uplift described within published works is further complicated with regard to attempting to identify regional uplift rates, because most of the south and east of Crete is affected by onshore and offshore faulting with the west of the island uplifted as a result of several Holocene earthquakes (Pirazzoli 1996; Shaw et al., 2008; Stiros, 2001, 2010). As such, Strobl et al. (2014) commented that the upper values of uplift are likely to be representative of the short-term (i.e. Holocene) and significantly over-estimate the Pliocene-Quaternary uplift rate. Along the south central area of Crete (Figure 1a), Gallen et al. (2014) suggests Late-Quaternary regional values of ~0.8 mm/yr. This value was obtained by first modelling the expected elevations of terraces in the hangingwall of the SCCF assuming there were no other uplift sources; to do this they assumed a fault-related subsidence versus uplift value of 4:1. These results were then compared to the measured elevations of the hangingwall and the difference was inferred to represent regional values. However, the impact in terms of uplift associated with the offshore upper-plate faults was not considered within their analysis, and as will be shown below, their time varying uplift and uplift values rely on ages they assigned to palaeoshorelines, some of which are questioned.

2.3 *Deformed marine terraces and their palaeoshorelines*

Quaternary marine terraces and their associated palaeoshorelines represent markers in the landscape that are produced during sea-level highstands associated with interglacial periods. The marine terraces and their associated palaeoshorelines become uplifted and preserved as a result of the interplay between eustatic sea-level change and tectonic uplift (Lajoie, 1986). They document long-term uplift and commonly occur where uplift due to repeated earthquakes outpaces sea-level change, and, as such are used to investigate fault-related deformation (e.g. Armijo et al., 1996; Lajoie, 1986; Roberts et al., 2009, 2013; Saillard et al., 2011; Tortorici et al., 2003; Westaway, 1993). A combination of geological knowledge and deformation of the palaeoshorelines associated with marine terraces can be used to explore the cause of uplift (Armijo et al., 1996; Gallen et al., 2014; Roberts et al., 2009, 2013). The marine terraces studied in this paper have previously been investigated by Angelier (1975b) and Gallen et al. (2014), and are broadly parallel to the coastline and in the case of the SCCF, parallel to the strike of the fault. Three possible pre-existing age controls from Gallen et al. (2014) have been obtained using OSL (Figures 3b-d). Two ages constrain the lowest palaeoshoreline to the 76.5 ka highstand (LS1251 and LS1254) in the western sector with the remaining sample (LS1255) (Figure 3) dating the lowest palaeoshoreline in the hangingwall of the SCCF to the 125 ka highstand (Gallen et al., 2014). In this study we are particularly interested in how uplift changes along and across the SCCF.

3. Methods

This research revisits known palaeoshorelines in southern Crete, previously investigated by Gallen et al. (2014), in order to conduct a reappraisal of palaeoshoreline ages. The field-based, DEM and dating methods we employed to carry out this investigation are detailed within this section with an explanation of our method in Figure 4. We show how new ages obtained using ^{36}Cl exposure dating are used to allocate highstands to palaeoshorelines throughout the research area and then discuss the uncertainties involved in the process.

3.1 *Collecting palaeoshoreline elevation data*

We collected palaeoshoreline elevations through a combination of study of a 5 m DEM (produced by ktimatologio SA from air-photo stereopairs) (Figures 2 and 3) and field work to verify the DEM data, elevations were obtained using a hand-held barometric altimeter which was regularly recalibrated. Palaeoshoreline elevations from 17 serial topographic profiles, taken perpendicular to the strike of the palaeoshorelines (Figure 3), were recorded and investigated; we avoided areas near river incision, preferring to use broad interfluves, to ensure marine and not fluvial features were measured. These palaeoshorelines were also investigated in Google Earth to check that the breaks of slope were not associated with 'man-made' features and, more importantly, they were verified during field mapping throughout 2016 and 2017 campaigns.

Field-based geomorphological indicators (Figure 5) used to identify palaeoshorelines include (a) notches (Ferranti et al., 2006), caves, lithophagid borings (Firth & Stewart, 1996; Papanikolaou et al., 2010; Roberts et al., 2013), (b) planed-off limestone and conglomeritic wave-cut platforms where bedrock, pebbles and cobbles were eroded by wave action (Roberts et al., 2009), and (c) millholes/potholes, that is, circular depressions in the platform caused by pebbles scouring the surface as a result of wave action (Miller & Mason, 1994). These features generally form in the intertidal zone, a few decimetres to metres down-dip of the actual palaeoshoreline. Marine sedimentary deposits are commonly deposited on wave-cut platforms and include algal reefs, which are suggestive of shallow water (Kershaw et al., 2005), conglomerates with rounded clasts and lithophagid and sponge bored pebbles, and coarse sands. It is common for these sedimentary deposits to be fossiliferous in places and contain serpulid worm tubes, various bivalve shells and rare corals (Angelier, 1979b; Gallen et al., 2014; Gaki-Papanastassiou et al., 2009; Strasser et al., 2011). Thus, the palaeoshoreline itself is commonly a break of slope marking a palaeo-rocky-shoreline or a palaeo sea-cliff that exists a few decimetres to metres up-dip of either a wave-cut platform or outcrops of shallow marine sediment.

3.2 *^{36}Cl sampling approach and preparation*

We have developed a method to use *in situ* ^{36}Cl cosmogenic exposure dating to define the ages of palaeoshorelines through identification of sites that indicate minimal erosion. ^{36}Cl exposure dating has historically been used to date features like fault scarps (e.g. Schlagenhauf et al., 2010) and exposure ages of glacial boulders (e.g. Ivy-Ochs et al., 2004), however, it has also been successfully used to date a Holocene-age marine platform in Scotland (Stone et al., 1996), inspiring our study. There are a number of natural pathways capable of producing ^{36}Cl in limestone (see Dunai, 2010 for details). The main production pathway in limestones is spallation of ^{40}Ca atoms which occurs predominantly in the top 2 m of rock beneath exposed limestone surfaces (Licciardi et al., 2008) and exponentially decreases with depth, while production as a result of low energy neutrons also contributes to the ^{36}Cl concentration (Schimmelpfennig et al., 2009).

We selected sample sites where we were confident of minimal erosion of the surface we were trying to date, indicated by preserved lithophagid borings and millholes (Figure 6a,c,h and i) as their preservation suggests erosion since palaeoshoreline formation of few centimetres or less.. Samples were removed using a mallet and chisel. Shielding values were noted every 30^{o} of azimuth as per the method in Dunai et al. (2010). Prior to ^{36}Cl sample preparation, all samples were analysed as thin sections to accurately determine their lithologies and washed in distilled water in an ultrasonic bath. We then followed the ^{36}Cl sample preparation method outlined by Schimmelpfennig et al. (2009). Following Accelerator Mass Spectrometry (AMS), the exposure ages of samples were calculated using CRONUScalc (Marrero et al., 2016), which calculates concentrations using known production pathways. A constant, and very low, value of 0.1 mm/ky for erosion was applied to all samples when calculating the ages in CRONUScalc, and this is further discussed in the results section below. Exposure age results are shown in Table 1.

3.3 *Assigning palaoeshorelines to highstands: the Terrace Calculator*

We use the so-called "synchronous correlation" approach to assign ages to un-dated palaeoshorelines (see Houghton et al., 2003, Roberts et al., 2009, Roberts et al., 2013, Meschis et al., 2018) (Figure 4). This approach makes use of the observation that Quaternary sea-level highstands occurred during unevenly spaced time intervals and have variable elevations relative to sea-level today. Correlation is aided if the age of one palaeoshoreline is known from absolute dating, and this is used to drive the simplest hypothesis, that of constant uplift-rate through time. Constant uplift-rate scenarios are tested before more complicated uplift scenarios are explored if needed. We initially use the age determinations from ^{36}Cl to drive the search for correlation between the measured elevations and those predicted from sea-level curve data. We apply the uplift rate implied by the ^{36}Cl age determinations to the entire sequence of palaeoshoreline elevations measured from a topographic profile (Figure 4a) and field data. This tests whether the elevations of un-dated palaeoshorelines can be explained by the uplift-rates implied by the elevations of dated palaeoshorelines. This calculation is facilitated by a 'Terrace Calculator' in Excel, populated with data from the sea-level curves (Rohling et al., 2014; Siddall et al., 2003). The calculator uses an input uplift rate (u), which is iterated, to calculate the predicted elevations (*Epred*) of all highstands using the age of the highstands (T) and the sea level elevations (SL) of the highstands relative to today's sea level (Eq.1):

$$E_{Pred} = (T \times u) + SL \qquad \text{(Eq.1)}$$

For this study the 'Terrace Calculator' has been extended beyond 410 ka (compare with Houghton et al. 2003, Roberts et al. 2009, 2013) to include highstands to 980 ka (Siddall et al. (2003) to 410 ka, Rohling et al. (2014) beyond 410 ka) so that we can explore the uplift further back in time.

The output of the 'Terrace Calculator', given iteration of the uplift rate, is a set of predicted elevations for all sea-level highstands along the topographic profile in question, which are then matched if they are ±10 m of the measured elevations allowing us to assign palaeoshorelines to highstand ages (Figure 4b). The fit between the two datasets (predicted versus measured elevations) was evaluated using R^2 and the Root Mean Square Error (RMSE). We also attempt to maximise the number of palaeoshorelines that we identify, taking particular care to make sure that palaeoshorelines that tend to have prominent geomorphology, such as those from 125, 240 and 340 ka, are identified. However, not all terraces will have preserved palaeoshorelines, either because they have been sub-aerially eroded, or eroded as a consequence of overprinting of older terraces by younger sea-level highstands (Jara-Muñoz et al., 2017; Jara-Muñoz & Melnick, 2015; Pedoja et al., 2017; Pedoja et al., 2014; Roberts et al., 2013). This is visible on Figure 4c where the Terrace Calculator shows which palaeoshorelines are likely to have been destroyed for profile 10 with an uplift value of 0.37 ± 0.09 mm/yr; palaeoshorelines at 175, 217 and 285 ka are particularly prone to being overprinted.

In order to assign highstand ages to undated palaeoshorelines we laterally traced dated palaeoshorelines and then tested all possible uplift scenarios based on the measured palaeoshoreline elevations. We used the number of matches between measured and predicted palaeoshoreline elevations and RMSE values to identify the best fit. Exact uplift values for each topographic profile were obtained by iterating the uplift values from 0.1 to 1.0 mm/yr at intervals of 0.05 mm/yr and plotting the RMSE values obtained from comparing the predicted versus measured elevation values. The uplift value with the lowest RMSE was applied to the topographic profile (see Figure 4d for an example).

3.4 *Uncertainties and errors*

Elevation measurement errors from the hand-held barometric altimeter used for field determination of palaeoshoreline elevation are ± 3 m, with errors of ± 4 m for the DEM (at 95% confidence level). Uncertainties for the exposure ages from ^{36}Cl exposure dating are calculated in CRONUScalc (Marrero et al., 2016) and rely on the uncertainty value for each input parameter. The uncertainties are reported as internal (analytical) and external (total) values in ka; internal uncertainty values are linked to analytical uncertainties and result in a minimum uncertainty age value. External uncertainties are calculated by propagating the production-rate and measured uncertainties and combining them with the analytical uncertainty (Marrero et al., 2016).

Sea-level curve uncertainties vary depending on the sea-level curve employed. For the Siddall et al. (2003) curve the reported uncertainty on the sea level is 12 m compared to the reported uncertainty of 6 m for the Rohling et al. (2014) curve. The uncertainty values on the age of the sea-level highstands are reported to be 4 ky from Rohling et al. (2014), but are not defined by Siddall et al. (2003). This value is needed in order to propagate our uplift rate errors so we assign the value obtained by Rohling et al. (2014) as this later work builds upon research initially based upon the Siddall et al. (2003) data. We used the equation for standard error (*SE*) to propagate our uplift value errors (Eq.2):

$$SE\ (u)^2 = u^2\left(\left(\frac{\sigma_{H^2}}{(H_T - H_{SL})^2}\right) + \left(\frac{\sigma_{T^2}}{T^2}\right)\right) \qquad \text{(Eq.2)}$$

Where SE is the standard error, u is the uplift rate, σ_H is the combined uncertainty for measured palaeoshoreline elevation and sea level relative to today, H_T is the measured palaeoshoreline elevation, H_{SL} is the sea level for the highstand in question, and, T is the highstand age related to the terrace formation. Overall, we think that summed errors are small relative to the signals we are trying to identify.

4. Results

This section applies the method outlined above to correlate sea-level highstand ages and palaeoshoreline elevations with absolute dating provided by *in-situ* ^{36}Cl exposure dating of wave-cut platforms and other published ages. We review the along-strike variation of palaeoshoreline elevations between the topographic profiles and evaluate the temporal and spatial variation of uplift values. We then use these data in combination with the palaeoshoreline elevations of offset terraces on the footwall of the SCCF to derive the throw rate and recurrence interval values for the fault.

4.1 *Field mapping and palaeoshoreline elevations*

Detailed field mapping of the study area reveals that the western section (Profiles 1-5; Figure 3b) displays excellent palaeoshoreline features cut into Mesozoic bedrock (Figure 7b-i) including notches and shoreline caves, many of which contain abundant lithophagid borings. Syn-wave-cut platform deposits are rarely preserved, except on the lower platform of Profiles 4 and 5, where cemented marine sands and conglomeritic deposits occur (Figure 6h). Extensive wave-cut platforms, that can be mapped for tens to hundreds of metres along strike, form laterally-persistent features in the landscape, and kilometres along strike on DEMs (Figures 3, 7a,b).

East of where the SCCF fault crosses the coast (Figure 3c-d), significant fluvial incision exists due to softer lithified syn-rift sediments with the creation of interfluves clearly visible in the DEM (Figures 2c and e, 3c and e). The soft sediments preserve breaks of slope marking the palaeoshorelines, especially on interfluves, and these can be mapped between profiles. Flat surfaces a few decimetres to metres down-dip of the palaeoshorelines are wave-cut surfaces cut into compositionally immature conglomerates containing bioclastic debris including marine oyster shells. In places bedrock limestone occurs as wave-cut platforms with associated sedimentary deposits (Figure 7e) or as sea-stacks which represent inliers within the shallow marine sediments and display horizontal stripes of lithophagid borings. Fault scarps are clear in the field (Figure 7a-ai) and on the DEM (Figure 3c and e) separating the hangingwall marine sediments from uplifted basement rocks.

During fieldwork we measured the elevations of as many palaeoshoreline elevations as we could access; ~30% of DEM inner-edges were verified in the field. The field and DEM elevations were well correlated with an R^2 of 0.999 (Supplementary Figure 1), and we interpret this to suggest that we have a robust regional coverage of palaeoshoreline elevations from our combined field and DEM studies. In summary, we mapped the palaeoshorelines and, in addition to the existing age controls from Gallen et al. (2014), obtained ^{36}Cl exposure dating results that place further constraints on the ages of the palaeoshorelines – these are discussed below.

4.2 *^{36}Cl exposure dating results*

Absolute dating of the wave-cut platforms was carried out using ^{36}Cl exposure dating. Five localities were sampled, the geomorphology of each sample location is detailed in Supplementary Table 1 and shown in Figure 6b and d. The ^{36}Cl exposure age values for each sample are reported along with their external errors in Figure 8a and Table 1. We believe that four of the five ^{36}Cl determinations provide exposure ages that can be assigned to sea-level highstands, whereas the fifth was probably covered by sediment at some point and a complex exposure–covering–re-exposure history results in an anomalously low ^{36}Cl concentration. The four exposure ages that we can assign to sea-level highstands are: S1, 134 ± 33 ky; S3, 61 ± 13 ky; S4, 88 ± 21 ky, and S5, 108 ± 24 ky. The fifth ^{36}Cl determination, S2, implies an exposure age of 40 ± 7.5 ka, but we reject this age because (a) there is no clear sea-level highstand at this time on the sea-level curve (Figure 8b), and (b) re-examination of our field photographs shows that the sample was taken close to syn-wave-cut platform sediments dated by Gallen et al. (2014) as 78 ±8 ka using OSL, and we now suspect our sample was covered by this sediment before erosion (Figure 6h), producing a low ^{36}Cl concentration and hence age.

While we recognise the value of the errors on our ^{36}Cl exposure age determinations is relatively large compared to other dating techniques, it is important to note that these are likely to be overestimated when comparing between groups of samples from a single geographic location where the uncertainties are not independent (Marrero et al., 2016). Despite the errors, we note that Table 1 shows that for the samples from close to TB (Figure 3) the concentration of ^{36}Cl atoms/g in the footwall samples (S3-S5 from profiles 4 and 5, Table 1) increase with elevation, as would be expected if the rocks were incrementally lifted out of the sea, suggesting a stratigraphical correlation of palaeoshoreline age with elevation.

The wave-cut platforms and associated palaeoshorelines are likely to have been formed during sea-level highstands which occurred at 76, 100, 125, 175, 200, 240, 310, 340 and 410 ka (Siddall et al., 2003) (Figure 8b); the question is which of these is the highstand for each wave-cut platform? Plotting the exposure ages against the sea-level curve shows that, samples could be allocated to more than one sea-level highstand (Figure 8b): S3 (61 ± 13 ka), inner edge 38 m, could be allocated to the 50 or 76.5 ka highstands; S4 (88 ± 21 ka), inner edge 67 m, could be allocated to the 76.5 or 100 ka highstands; S5 (108 ± 24), inner edge 116 m, could be allocated to the 100 or 125 ka palaeoshoreline, and, S1 (134 ± 33 ka), inner edge 54 m, could be allocated to the 125 highstand.

Samples close to TB (S3, S4 and S5) were removed from sequentially higher terraces which form a set of continuous palaeoshorelines along Profiles 4 and 5 situated 50 m apart (Figures 3d, 7b). These samples are interpreted to represent three successive wave-cut platforms and their associated palaeoshorelines at 38, 67 and 116 m. There is no evidence of additional palaeoshorelines existing between these elevations (see Figure 7b). Having identified the possible highstands each sample might belong to (Figure 8b) we tested all synchronous correlation uplift-rate scenarios and found that one uplift solution of 0.89 ± 0.09 mm/yr results in the allocation of all of the exposure ages and their palaeoshorelines to three sequential highstands, the 76.5, 100 and 125 ka. The results of the other tested scenarios are shown in Supplementary Figure 2 (for the 76.5, 100 and 125 ka highstands) and detailed in Supplementary Table 2 (for all highstands to 980 ka). Our allocation of the lowest palaeoshoreline to the 76.5 ka highstand is in agreement with the OSL age from syn-wave-cut platform deposits obtained by Gallen et al., (2014) (sample LS1254) but the two studies do not agree with regard to the palaeoshoreline elevation for this location (27 m from Gallen et al. (2014), 38 m this study). We cannot explain this variation between palaeoshoreline measurement and base our 38 m palaeoshoreline measurement on the geomorphic observations we made in the field along with the absolute dating from Gallen et al., 2014 (25 m) and from this study (34 m) which both suggest a highstand age of ~76.5 ka

For ^{36}Cl sample S1, sampled from the hangingwall (Figure 3c), the exposure age of 134 ± 33 suggests that it should be allocated to the 125 highstand which requires an uplift value of 0.37 mm/yr ± 0.09.This is in agreement with the 125 ka OSL age obtained by Gallen et al., 2014 (sample LS1255) for the same palaeoshoreline 3 km to the west (Figure 3c). A final note is that calculating the ^{36}Cl exposure ages of these samples relies on CRONUScalc (Marrero et al., 2016), which requires an erosional rate value for each sample. Based on the fact that all of these samples are from the same bedrock limestone lithology, with widespread preservation of lithophagid borings that are a few centimetres deep when formed, the same erosional rate of 0.1 mm/ka was applied. Over 125 kyrs, 1.25 cm would be eroded, consistent with the preservation of lithophagid borings.

4.3 *Temporally constant uplift rates*

Absolute ages in combination with the Terrace Calculator are used to iterate uplift rates to produce a correlation between mapped palaeoshorelines to expected highstand elevations for un-dated palaeoshorelines. An outcome of this correlation is an uplift rate for each of the 17 topographic profiles (Figure 9). This in turn allows us to investigate palaeoshoreline elevations and uplift-rates along strike.

In general, we achieve a good fit between inner edges identified in the field and on the DEM, with palaeoshorelines at the elevations expected given our preferred uplift rate scenarios. The most prominent palaeoshorelines on the sea-level curve (125, 200, 240 and 340 ka) fall on clear geomorphic inner edges on the topographic profiles in most cases, and other more-subtle sea-level highstands (e.g. 76 ka and 410 ka) are also identified in places. Cross-plots of measured inner-edge elevations against predicted inner-edge elevations from the Terrace Calculator (Figure 10) show an R^2 value of 0.9996. This value confirms that the fits between highstands and palaeoshorelines are good, giving confidence to the uplift rates. Figure 9 shows that constant uplift rates through time produce excellent fits between measured and predicted palaeoshoreline elevations. This contrasts with the interpretation from Gallen et al. (2014) who suggest uplift rates increased through time. This contrast is probably due to the fact that Gallen et al. (2014) lacked the age control that our new cosmogenic exposure ages provide near to TB, and also because they used a sequential correlation technique to derive the ages of un-dated palaeoshorelines (see Roberts et al. 2013 for a critique of this approach). The major consequence of the sequential approach is that as uplift rates are calculated for each palaeoshoreline within a topographic profile. Any incorrect allocation between palaeoshoreline to highstand may result in variation between uplift rates along one topographic profile, which could be erroneous.

Further variation between the two studies occurs when the comparing the allocation of highstands to palaeoshorelines, this is particularly visible along Profiles 4, 14 and 17. Specifically, along Profile 4 we allocate the 125, 200, 285, 340, and 410 ka highstands to palaeoshoreline elevations at 116, 173, 224, 310 and 360 m. Along the same profile, Gallen et al. (2014) allocated the following palaeoshoreline elevations to the same highstands, respectively: 97, 140, 166, 210, 251 m. For profile 14, we place the 125, 200 and 340 ka palaeoshorelines at 41 m, 53 m and 94 respectively while Gallen et al. (2014) have the same palaeoshoreline ages allocated to palaeoshoreline elevations of 1 m, 39 m and 50 m. There is a similar pattern along Profile 17 where we allocate the 125, 200 and 340 ka highstands to 33, 43, and 85 m and Gallen et al. (2014) suggest the same highstands are at 2, 40 and 59 m. For Profiles 9 and 13 the variation between the two studies is only apparent for older highstand allocations (see Table 2).

The reason for the highstand to palaeoshoreline variation could be due to measurement differences, sea-level curve data or the method employed to allocate palaeoshorelines to highstands. While there is generally good agreement between the measured palaeoshoreline elevations in this study and those obtained by Gallen et al. (2014) (50% of our measurements are within ±7 m with those from Gallen et al. (2014)), we suggest that some of the variation is due to different measurements. We do not think that the fact that different sea-level curves for 0-450 ka are used between the two studies (Siddall et al., 2003 for this study, Lambeck and Chappell, 2001 for 0-125 ka and Waelbroeck et al. (2002) for 125-410 ka (Gallen et al., 2014)) has a significant impact, but that it is linked to the fact that Gallen et al. (2014) recognise only one of the MIS 7 highstands (215 ka) from Waelbroeck et al. (2002) (compare this to the 200 ka, 217 ka and 240 ka highstands used in this study). However, to ensure we have been rigorous in our approach we explore the effect of other sea-level curves on our results by plotting predicted elevations from Siddall et al. (2003) for all

17 profiles against the predicted elevations from other sea-level curves (Supplementary Figure 3) (Lambeck and Chappell, 2001; Shakun et al, 2015 and Spratt and Lisiecki. 2016; Waelbroeck et al., 2002). These plots show variations for the elevations belonging to the ~76.5 ka, ~217 ka, ~280 ka, ~340 ka highstands along profiles 1-5 in the western section, but as a result of lower uplift rates, the variation is less pronounced in the eastern section (profiles 6-17). We note that from profiles 14-17 the youngest palaeoshoreline for all sea-level curves is predicted to be the 125 ka (Supplementary Figure 3, profiles 14-17).

Further analysis using sea-level data from Waelbroeck et al. (2002) in place of Siddall et al. (2003) was carried out for each topographic profile in order to explore the effect this had on the uplift rates (Supplementary Figure 4). The results show an almost identical spatial variation of uplift rates across the 17 topographic profiles (see Figure 9 for the uplift rates obtained using Siddall et al. (2003)). There is some very slight variation of the uplift rates; for profiles 1-6, this variation does not exceed 0.04 mm/yr and for profiles 6-17 it does not exceed 0.02 mm/yr. This is a consequence of the fact that the Siddall et al. (2003) and the Waelbroeck et al. (2002) curves are broadly similar for the key highstands. Relative highstand sea levels differ by 1 m for the 125 ka, 5 m for the 200 ka, 5 m for the 240 ka and 1 m for the 340 ka.

Our constant uplift rate interpretation is preferred because (a) it is simpler, (b) it identifies geomorphic features that are consistent with both the prominent and less prominent sea-level highstands, and (c) we have mapped a greater number of palaeoshoreline elevations using the high-resolution DEM. To further explore the constant uplift rate, we plotted each profile’s highstand ages versus measured elevations. These plots result in near-straight lines for all of the 17 profiles which strongly support temporally constant uplift (Figures 11a-p) (note we do not expect perfectly-straight lines due the variations in palaeo-sea-level between highstands). For the topographic profiles along the western footwall section (Profiles 1-5, Figures 11a-e) constant uplift rates are implied to 600 ka and in the case of profile 1, up to c. 900 ka. Along the hangingwall section (Profiles 6-17, Figures 11f-p), constant uplift rates are implied up to 410 ka.

4.4 *Along strike variation of palaeoshoreline elevations and uplift*

When the elevations for the palaeoshorelines are plotted along strike across the entire area the variation in uplift either side of the western tip of the SCCF is clearly visible (Figures 12, 13a-b), also pointed out by Gallen et al., (2014). Palaeoshorelines in the hangingwall of the SCCF, east of ~22.5 km (Figure 12) (longitude 25.28º) along strike, are relatively low and closely spaced in elevation, whilst those to the west in the adjacent footwall and beyond the SCCF fault tip are higher and more widely-spaced with elevation.

Within the western sector, elevations, and therefore uplift (Figure 12, 13a), increases across Profiles 1 to 5 (from west to east) where it reaches a peak at 0.89 ± 0.09 mm/yr. This pattern of uplift is observed on all palaeoshorelines throughout the area and is particularly reliable given that there are age controls at the western and eastern areas within this sector (see samples LS1251 and S3 on Figure 12a). We interpret the spatial variation in the uplift rates along the western sector as footwall uplift.

For the SCCF, the transition from footwall to hangingwall at TB results in uplift rates decreasing from 0.88 ± 0.08 mm/yr (Profile 5) to 0.39 ± 0.08 mm/yr (Profile 6) (Figures 13a-b; Table 2). They continue to decrease to the east toward the centre of the SCCF at Profile 17; the lowest palaeoshoreline allocated to the 125 ka highstand decreases in elevation from 55 m to 33 m. Uplift rates decrease from 0.39 ± 0.08 mm/yr to 0.24 ± 0.09 mm/yr, with lowest values between Profiles 14 and 17 at the centre of the fault where the displacement, and hence the component of hangingwall subsidence is at its greatest. This deformation suggests a component of hangingwall subsidence as a result of normal-slip motion of the SCCF, but as the hangingwall terraces are above current sea-level we can conclude that this area is being uplifted by a background value, perhaps related to the subduction interface, thrust faulting in the wedge above the subduction interface, or offshore upper-plate faults, that exceeds the subsidence value linked to the SCCF.

The variation of uplift rates between the western (Figure 13a) and eastern (Figure 13b) sections is a clear indication that the SCCF has been active in the Late Quaternary. Earthquakes along the SCCF during the Late Quaternary would result in greater cumulative fault offset, it follows that older palaeoshorelines would therefore experience more deformation. Due to variation in displacement along fault strike, older palaeoshorelines are expected to be more steeply tilted along-strike than younger, lower palaeoshorelines. To test this we have measured the tilt angle for each palaeoshoreline from its tip to the centre (highest point for the footwall and lowest point for the hangingwall (Figure 12a). These data for measured tilt angles are plotted for each palaeoshoreline on the footwall and adjacent hangingwall (Figures 13c and 13d respectively, Supplementary Figure 5).

The tilt values increase with age, suggesting that the older palaeoshorelines have experienced more fault-related deformation (uplift in the case of the footwall; subsidence, in addition to some uplift component, in the case of the hangingwall). Note that the sharp increase of the tilt value observed between the 125 ka and 525 ka palaeoshorelines along the western sector between Profiles 1 and 5 (Figure 13c) occurs as a result of a lack of continuous elevation data for the palaeoshorelines in between. Also note that the values of tilt observed for the footwall and hangingwall are similar which is perhaps unexpected given the fact that observations from other normal fault systems suggest the amplitude of deformation tends to be greater in the hangingwall compared to the footwall, with ratios in the order of ~1:2-3 uplift to subsidence (McNeill and Collier, 2004; Papanikolaou et al., 2010*)*. When we compare the hangingwall tilt angles for the SCCF (0.16 along the 340 ka terrace), against other hangingwall tilt angle values from elsewhere in the Mediterranean: 0.93 and 2.14 along the 340 ka terraces belonging to the Capo D'Orlando fault, Sicily (Meschis et al., 2018) and the Vibo fault, Calabria (Roberts et al., 2013) respectively, the SCCF has anomalously low values. As all normal faults ought to have similar displacement gradients (e.g. see Schlische et al. 1996), this is unusual. The reasons for the relatively low tilt angles are explored further in the Discussion section.

4.5 *Calculating the throw rate of the SCCF*

We can use the hangingwall exposure ages and along-strike highstand-to-palaeoshoreline allocation to investigate faulting activity on the SCCF. Profile 14 is located toward the centre of the fault (Figure 3e) along an interfluve that abuts against the fault scarp (Figures 7a and 9p). Directly above the scarp in the footwall, six palaeoshorelines are observed from the DEM topographic profile; the lower three were explored during fieldwork and show wave-cut platform evidence including syn-wave cut platform deposits, possible lithophagid borings, and a notch. The hangingwall of this profile displays four preserved palaeoshorelines which have been allocated to highstands by laterally tracing the palaeoshorelines within the DEM from the absolute dating of the 54 m palaeoshoreline on Profile 10 (Figure 9l). The oldest and highest marine terrace on the hangingwall along Profile 14 is modelled to extend from ~130 m to ~162 m in elevation and belong to the 478 ka highstand. This terrace has experienced faulting, as indicated by lithological variation across the fault (IGME map sheet Ano Viannos 1:50,000), and its predicted palaeoshoreline elevation is suggested to be at an elevation where the main fault scarp of the SCCF is observed. This indicates that the 478 ka terrace may have been offset by the SCCF placing the 478 ka palaeoshoreline on the uplifted footwall and allows us to calculate the throw rate of the SCCF.

As we have measured elevations of palaeoshorelines on the footwall above the scarp in this location, we can test whether this plausible using the Terrace Calculator. The lowest observed (field and DEM) palaeoshoreline on the footwall was at 336 m**.** Allocating the 336 m palaeoshoreline to the 478 ka highstand requires an uplift rate of 0.71 ± 0.02 mm/yr which we apply to the entire footwall topographic profile. The predicted elevations for highstands >478 ka using the 0.71 mm/yr uplift rate matches all six of the measured palaeoshoreline elevations along this profile (Table 3; Supplementary Figure 6a). In order to ensure that we have identified a good fit between palaeoshoreline elevations and highstand ages along the footwall profile, we modelled all possible scenarios by testing how well the measured and predicted palaeoshoreline elevations matched if we allocated, in turn, each highstand older than 478 ka to the lowest footwall palaeoshoreline (336 m). The results show that allocating the 478 ka highstand to the palaeoshoreline at 336 m yields the highest number of matches between the predicted and measured palaeoshoreline elevations (Supplementary Table 3; Supplementary Figure 6b).

We therefore suggest that the 478 ka terrace has been offset by the fault and we can use the 196 m of measured vertical fault displacement (Figure 12) to calculate a throw rate of 0.41 mm/yr, which equates to a slip rate of 0.58 mm/yr (the average dip of the fault is 45º). The throw rate value, in addition to the expected coseismic displacement obtained from empirical fault-scaling relationships (Wells and Coppersmith, 1994) can be used to calculate the time-averaged recurrence interval on the fault. The recurrence interval is an indication of the time interval that may occur between earthquakes on the same fault of a similar magnitude. A typical Mw 6.5 earthquake along the SCCF would result in a maximum vertical surface displacement of ~1.1 m (Wells & Coppersmith, 1994), which assumes the occurrence of ~178 standard earthquakes along the length of the fault over 478 ka resulting in a time-averaged recurrence interval of ~2685 years. This approach is based upon the constant-length fault model proposed by Walsh et al. (2002) that suggests that fault lengths are established from an early stage and growth is achieved via cumulative displacement.

5. Discussion

We have shown that differential uplift occurs along the south central area of Crete, but that while this uplift varies spatially it appears to have been temporally constant between 76.5-980 ka. We have observed that the uplift rate varies along the strike of a mapped fault, and across the fault as seen through a change in uplift rate between the western footwall section and hangingwall of the SCCF. Our major conclusion is that normal faulting must be included in any analysis of the uplift, and hence dynamics, of the tectonics for Crete, the HSZ, and perhaps other subduction systems.

In detail, it is now clear that limestone wave-cut platforms, which display features suggesting minimal erosion, can be used to provide cosmogenic exposure ages that correlate with highstands from Quaternary sea-level curves, and hence constrain the rates of uplift. This may have wider significance because experience suggests to us that wave-cut platforms amenable to *in situ* ^{36}Cl cosmogenic exposure dating appear to be more common than sites containing corals suitable for $^{234}U/^{230}Th$ dating or sediments suitable for OSL dating, so the former approach may allow many more sites to be dated, and across wider regions. The success of the ^{36}Cl approach relies on careful site selection to ensure that samples are removed from locations that display features indicative of minimal erosion such as lithophagid borings and millholes with further consideration as to the possibility of sedimentary cover. We also advocate checking the consistency of the implied ages with other un-dated palaeoshorelines in the same across-strike profile using the synchronous correlation approach because this quantifies the goodness of fit to all mapped palaeoshorelines simultaneously, and is less prone to subjective interpretations that may suffer from preconceptions about the uplift history.

The variation in uplift-rate along-strike of the SCCF is reminiscent of similar observations for other active faults. Specifically, spatial variation in footwall uplift responsible for deforming palaeoshorelines has been reported in the Gulf of Corinth along the South Alkyonides fault (Morewood & Roberts, 1999; Roberts et al., 2009), the Eastern Eliki fault (McNeill et al., 2005) and the Xylocastro fault (Armijo et al., 1996). Along strike variation in uplift rate along the hangingwall of normal faults has been reported along the Vibo fault in Calabria (Roberts et al., 2013), and along the Capo D'Orlando and Messina Straits faults in Sicily/Calabria (Cucci et al., 1996, Meschis et al. 2018). All the above examples show decreases in uplift or subsidence of palaeoshorelines towards fault tips with maxima near the centres of the faults. This observation links the structural geology of the faults with the uplift/subsidence pattern and hence supports the notion that normal faulting is a major control of vertical motions in the upper plate of subduction zones.

There are two aspects of our findings that are of particular interest. Firstly, uplift of the western section of the coast, between Profiles 1-5, is up to ~20 km away from the SCCF, so foowall uplift as a consequence of the SCCF alone is perhaps unlikely to explain the observed uplift. Secondly, we note very low along-strike tilt angles for the palaeoshorelines in the hangingwall of the SCCF compared to other examples (Roberts et al. 2013, Meschis et al. 2018). We quantitatively explore these issues via calculations of elastic interaction and discuss the outcome of each in turn.

5.1 *Exploring the uplift caused by extensional upper-plate faulting using an elastic half-space model*

In this section we investigate whether the south-dipping normal faults immediately offshore of Crete and the transtensional Ptolemy fault play a significant role in affecting local uplift onshore; specifically, the extent that these faults impact (i) uplift of the western footwall section (Profiles 1-5), and (ii) the low tilt angles observed on the palaeoshorelines in the hangingwall of the SCCF (profiles 6-17) where the SCCF exhibits a 0.16^{o} along-strike tilt angle for the 340 ka hangingwall palaeoshoreline (Figure 13d). This value can be compared to the tilt angles on other 340 ka palaeoshorelines in Italy (Vibo fault, Calabria) and Sicily (Capo D'Orlando fault) which have values of 2.15^{o} (Roberts et al., 2013) and 0.93^{o} (Meschis et al., 2018) respectively. The variation between these angles is unknown but may relate to fault interaction and differences in slip rates.

We model the coseismic uplift expected from upper-plate faults using Coulomb 3.3 software which allows the user to explore vertical fault-related deformation using inputs from multiple faults (Lin & Stein, 2004; Mildon et al., 2016; Toda et al., 2005). Fault traces and fault geometry input parameters (Table 4) were used in Coulomb to produce the vertical deformation expected during one earthquake along each fault, and we included the along-strike variability in fault strike using the code from Mildon et al. (2016). The sub-surface slip for each fault is an input within the Coulomb code and was iterated until the maximum Mw from Wells and Coppersmith (2004) was achieved (based on total fault-length scaling relationships); the output is a map view model of 2D deformation shown as vertical contours (Figure 14). We have chosen to model the Ptolemy trench fault with a seismogenic layer of 30 km based upon the microseismicty shown in Meier et al. (2004). We also modelled the deformation of the fault with a 15 km seismogenic layer and note that the footwall vertical deformation between the two models is similar. We recognise that this approach does not take into account post-seismic deformation as a consequence of faulting. However, it is suggested that postseismic deformation increases the magnitude of vertical motions by at most a few tens of percent of the coseismic values, and that postseismic vertical motions share similar spatial variation patterns as coseismic motions (Atzori et al. 2008; D'Agostino et al. 2012). The results of our solely coseismic models, assuming that the uplift:subsidence ratio is correct, provides qualitative insights into the absolute values for vertical motions. These analyses allow us to explore whether the influence of the offshore faults is capable of causing the observed uplift of the western section and if it tends to increase or decrease the tilt angles of the SCCF hangingwall onshore.

We first address the possible mechanisms that could be responsible for uplifting the western footwall section (Profiles 1-5): the results from the Coulomb modelling show that rupturing the Ptolemy fault results in 0.3-0.4 m of footwall uplift along the coastline from Profiles 1-5 (Figure 14a) compared to 0.01-0.02 m at the same location when we model the rupture of the offshore Cape Lithino normal faults (Figure 14b). We can attempt to differentiate between these two scenarios by calculating the implied recurrence interval for uplift events using the dated elevations of palaeoshorelines and the single earthquake uplift contours modelled in Coulomb (Figure 14a-b). At profile 2 on Figures 14a and b the 25 m palaeoshoreline has been allocated to the 76.5 ka highstand (using OSL dating of sample LS1251 from Gallen et al., 2014). Solely rupturing the Ptolemy fault results in 0.4 m of uplift at profile 2 (Figure 14a); over the period of 76.5 ka 62.5 standard earthquakes would be required for this palaeoshoreline to reach its 25 m elevation; this results in a time-averaged recurrence interval of 1224 years (Figure 14c) for Mw 7.3 events (this value is obtained from fault length-scaling relationships from Wells and Coppersmith, 1994; Table 4). We carried out the same analysis using the uplift produced by rupturing the western and eastern Cape Lithino faults which results in 0.018 m uplift per standard earthquake at profile 2 (Figure 14b). Over 76.5 ka 1389 earthquakes would be required to uplift the palaeoshoreline to 25 m, which results in a time averaged recurrence interval of 55 years (Figure 14d) for Mw 6.1

(western fault) and Mw 6.25 (eastern fault) events (Table 4). If we consider that 50% of the uplift was achieved postseismically, our recurrence intervals for the Ptolemy and Cape Lithino faults increases to 1838 and 83 years respectively (Figures 14e, f).

An analysis of the instrumental seismology for depths ≤30 km reveals a small number of moderately sized earthquakes (~Mw 5) which may be attributed to the Cape Lithino faults from a record that is thought to be complete since ~1900 (Dziewonski et al., 1981; Ekström et al., 2012; International Seismological Centre (ISC), 2016; Makropoulos et al., 2012; National Observatory of Athens (NOA), 1997; Papazachos et al., 1998); but there is no instrumental evidence of earthquakes ≥Mw 6.1 during this period. It is, therefore, possible that the Ptolemy fault could solely be responsible for uplifting the western section, because it is plausible that the Ptolemy fault may not have ruptured in this time period (i.e. 1900-2018). However, we suggest that the normal offshore faults alone cannot because the instrumental and historical seismicity do not support such a frequent earthquake recurrence on these faults.

To explore the impact of earthquakes along the offshore south-dipping normal Mirto fault and the transtensional Ptolemy fault on the tilt angles of the palaeoshorelines in the hangingwall of the SCCF (Profiles 6-17) we individually ruptured each fault and assessed the coseismic uplift pattern along profiles 6-17 (Figures 13a and b). We tested two iterations for the offshore Mirto fault – as one fault, and also as as two separate faults because there is a lack of clarity in the literature. Modeling the Coulomb footwall uplift for both fault options results in a coseismic uplift value of ~0.07 mm/yr (combined faults) versus ~0.02 mm/yr (two separate faults) at profile 10; as these values are in the same order of magnitude we use the combined fault model in the following analysis. As we are exploring the observed shallowing of tilt angles along the SCCF hangingwall palaeoshorelines from its western tip (Profile 6) toward its centre (Profile 17), we are interested in whether the footwall uplift from rupturing the Mirto and/or Ptolemy fault results in uplift patterns which increase or decrease toward the centre of the SCCF hangingwall. A coseismic uplift pattern which decreases from the western tip to the centre would increase the tilt angles along the SCCF hangingwall; an uplift pattern which increases from the western tip to the centre of the SCCF hangingwall would shallow the original tilt angles. Our modelling shows that when we compare footwall uplift caused by slip along the Ptolemy fault versus the Mirto fault, both result in spatially variable uplift but the magnitude and pattern of uplift differs. The Ptolemy fault results in maximum uplift values close to the centre of the fault at the western tip of the SCCF hangingwall (Profile 6), that decrease toward the east and centre of the SCCF (Profile 17) (Figure 14a). The coseismic uplift caused by the offshore Mirto fault results in maximum uplift values at the centre of the SCCF (Profile 17) that decrease toward the west (Profile 6) (Figure 14b). When we consider these uplift patterns in the context of a significantly shallower tilt angle along the SCCF hangingwall, (Figure 13d), we infer that it is plausible that the shallower tilt of the SCCF hangingwall palaeoshorelines could be linked to footwall uplift caused by the Mirto fault which uplifts the centre portion of the SCCF hangingwall by greater amounts than the tip areas.

Our interpretation of the Coulomb modelling is (i) that the Ptolemy fault may be solely capable of causing the observed uplift along the western section of the research area (Profiles 1-5), but it is also possible that uplift from the Cape Lithino faults makes a minor contribution; (ii) that the tilt variation observed along the palaeoshorelines in the hangingwall of the SCCF may be explained by uplift along the footwall of the offshore Mirto fault, with the relationship between faulting on the Ptolemy and Mirto faults difficult to disentangle with our modelling approach – the impact of the Mirto fault may be greater due to a shorter recurrence interval compared to the Ptolemy, but this needs more investigation; (iii) while we cannot constrain the individual long-term uplift contributions made by the Ptolemy and offshore normal faults, they all probably contribute to the observed temporally constant Late

Quaternary uplift within the research area, and, (iv) the upper-plate faults have the capacity to significantly peturb patterns of spatial variation in uplift (Figure 15). Importantly, these results show that elastic interaction between upper-plate faults is possible and may affect the coastal topography along the south central area of Crete; this is in contrast to the suggestions by other authors (Gallen et al., 2014; Mouslopoulou et al., 2015a) that regional uplift controls the observed coastal topography.

Our discusssion above suggests that both the onshore SCCF and the offshore faults are active and contributing to seismic hazard. Specifically, (i) the observed bedrock fault scarps along the SCCF likely record faulting since the Last Glacial Maximum (~12-18 ka) (Armijo et al., 1992; Benedetti et al., 2002; Palumbo et al., 2004; Roberts & Michetti, 2004), and, (ii) the youngest palaeoshorelines on the hangingwall (125 ka) and western footwall (76.5 ka) sections have been successively deformed by faulting since their formation; both these observations suggest active faulting on the SCCF. For the offshore faults, activity is supported by observations from seismic reflection and bathymetric studies that show that the upper-plate faults offset the sea-bed and control the basin development in the south of Crete (Alves et al., 2007; Alves et al., 2014; Kokinou et al., 2012). Based on fault length-scaling relationships (Table 4) (Wells & Coppersmith, 1994), we calculate that the SCCF is capable of a ~Mw 6.5 and the offshore normal and Ptolemy faults are capable of earthquakes in the region of Mw 6 and Mw 7.3 respectively.

The above observations suggest active extensional faulting within the upper plate of the subduction interface on Crete, and this should not be a surprise as a similar pattern has been described from other subduction zones. For example, differential uplift as a result of forearc extension is observed in Peru (Saillard et al., 2011), Costa Rica (McIntosh et al., 1993; Sak et al., 2009) and along the Calabrian Arc, where sets of normal faults control the local topography, (Meschis et al., 2018; Michetti et al., 1997; Papanikolaou & Roberts, 2007). Normal faults within the accretionary prisms in the upper plates of subduction zones have also been suggested to rupture during tsunami-inducing interplate earthquakes in Japan, Indonesia and Nicaragua (see McKenszie and Jackson, 2012, and references therein). The impact of upper-plate extensional faults must be considered when conclusions about slip distribution along the subduction interface are formed.

5.2 *Extension in the upper-plate of the Hellenic subduction zone*

Extensional faults that trend parallel to the Hellenic arc, such as those discussed in this study, exist offshore and onshore southern Crete (e.g Sfakia fault, Selia/Assomatos faults, Figure 1a), Kythira, the Mani Peninsula (Peloponnese), and western Peloponnese (Armijo et al., 1992; Gaki-Papanastassiou et al., 2011; Kassaras et al., 2018; Kokinou & Kamberis, 2009; Mascle et al., 1982; Papanikolaou et al., 2007; Papoulia et al., 2014; Papoulia & Makris, 2004; Tsimi et al., 2007; Wardell et al., 2014) and are in many places associated with uplifted marine terraces (e.g. Angelier, 1979a; Athanassas & Fountoulis, 2013; Gaki-Papanastassiou et al., 2011; Kelletat et al., 1976). The presence of terraces and onshore/offshore extensional faults throughout the rest of the Hellenic Arc leads us to suggest the observed uplift along these coastlines could, in part, also be controlled by upper-plate faults; there is evidence that terraces along the western Peloponnese are on a length scale associated with upper-plate extensional faults (Howell et al., 2017).

Convergence-based tectonic models for the south of Crete have suggested slip on shallow splay or steeply dipping thrust faults beneath Crete as the cause of coastal uplift; these are predominanty based on coastal observations along south western Crete linked to the 365 A.D. earthquake (Mouslopoulou et al., 2015a; Shaw et al., 2008; Taymaz et al., 1990; Tiberti et al., 2014). However, such convergence-based models have been extended throughout south Crete to explain the observed coastal topography (Mouslopolou et al., 2015a) without considering the impact of extensional faults within their analyses.

We suggest that in order to fully examine the mechanisms involved in long-term uplift, as opposed to single event uplift, it is essential to identify rates that can be robustly extended into the Late Quaternary. We believe that the results of this study show that that upper-plate extensional and transtensional faulting may peturb the uplift signals along the Hellenic arc and that studies throughout the Hellenic subduction zone, and other Worldwide subduction zones which use uplifted coastal marine terraces to make inferences about the causes and extent of subduction-related uplift, must ensure that they consider the role of upper-plate extensional faults in their analysis.

6. Conclusions

1. The deformation caused by extensional faulting in the upper plate of the HSZ, and possibly other upper plates worldwide, may be observed on the length scales of normal faults and are likely to peturb uplift rates that may be assumed to occur from slip on the subduction interface. We suggest that uplift contributions made by upper-plate faults should be considered when conclusions about subduction interface slip are made using coastal uplift observations.
2. The south central part of Crete is being uplifted as a consequence of upper-plate faulting combined with subduction-related (regional) uplift (Figure 15). Temporally constant uplift rates can successfully be used to explain the observed elevations of palaeoshorelines up to 900 ka in places. The observed spatial variation of uplift rates has been shown to be as a result of slip along upper-plate extensional faults.

3. ^{36}Cl cosmogenic exposure dating of wave-cut platforms, in combination with sea-level highstand data, is an acceptable method to derive uplift values over the long term and obtain Late Quaternary ages of palaeoshorelines. We emphasise the importance of sampling in locations with minimal erosion and note the significance of features such as lithophagid borings when carrying out site selection.
4. The SCCF is an active fault capable of a maximum Mw ~6.5 earthquake; it has a throw rate of 0.41 mm/yr, which equates to a slip rate of 0.58 mm/yr. Using empirical fault-scaling relationships, we calculate a recurrence interval of ~2700 years.

Acknowledgements

Fieldwork for JR was part-funded via the Tim Newling fund, Birkbeck College, University of London. AG was funded by project HELPOS "Hellenic Plate Observing System" (MIS 5002697). ^{36}Cl exposure dating was carried out at the Scottish Universities Environmental Research Centre (SUERC) and funded via CIAF grant 9161-1015. We thank Hellenic Cadastre SA for DEM data. Sincere thanks to Christina Tsimi (NOA) for customising the 5 m Digital Elevation Models for the research area. Thanks also to Zoe Mildon for sharing her modified Coulomb code. All data for this paper are appropriately cited and referred to in the reference list and available from Tables 1 and 2 and Figure 9. These data can be used to reproduce the results. This paper has benefited from comments by one anonymous reviewer and Gino de Gelder.

References

Alves, T. M., Lykousis, V., Sakellariou, D., Alexandri, S., & Nomikou, P. (2007). Constraining the origin and evolution of confined turbidite systems: Southern Cretan margin, Eastern Mediterranean Sea (34°30-36°N). Geo-Marine Letters, 27(1), 41–61. https://doi.org/10.1007/s00367-006-0051-1

Alves, T. M., Kokinou, E., & Zodiatis, G. (2014). A three-step model to assess shoreline and offshore susceptibility to oil spills: The South Aegean (Crete) as an analogue for confined marine basins. Marine Pollution Bulletin, 86(1–2), 443–457. https://doi.org/10.1016/j.marpolbul.2014.06.034

Angelier, J. (1979a). Recent quaternary tectonics in the hellenic arc: Examples of geological observations on land. Developments in Geotectonics, 13(C), 267–275. https://doi.org/10.1016/B978-0-444-41783-1.50043-X

Angelier, J. (1979b). Néotectonique de l'arc égéen.These d'etat. University de Paris VI, 405pp

Angelier, J., Lybéris, N., Le Pichon, X., Barrier, E., & Huchon, P. (1982). The tectonic development of the hellenic arc and the sea of crete: A synthesis. Tectonophysics, 86(1–3). https://doi.org/10.1016/0040-1951(82)90066-X

Armijo, R., Lyon-Caen, H., & Papanastassiou, D. (1992). East-west extension and Holocene normal-fault scarps in the Hellenic arc. Geology, 20(6), 491–494. https://doi.org/10.1130/0091-7613(1992)020<0491:EWEAHN>2.3.CO;2

Armijo, R., Meyer, B., King, G. C. P., Rigo, A., & Papanastassiou, D. (1996). Quaternary evolution of the Corinth Rift and its implications for the Late Cenozoic evolution of the Aegean. Geophysical Journal International, 126(1), 11–53. https://doi.org/10.1111/j.1365-246X.1996.tb05264.x

Athanassas, C., & Fountoulis, I. (2013). Quaternary neotectonic configuration of the southwestern Peloponnese, Greece, based on luminescence ages of marine terraces. Journal of Earth Science, 24(3), 410–427. https://doi.org/10.1007/s12583-013-0334-1

Atzori S., M. Manunta, G. Fornaro, A. Ganas, S. Salvi, 2008. Postseismic displacement of the 1999 Athens earthquake retrieved by the Differential Interferometry by Synthetic

Aperture Radar time series, Journal of Geophysical Research, 113, B09309, doi:10.1029/2007JB005504

Becker, D., & Meier, T. (2010). Seismic slip deficit in the southwestern forearc of the hellenic subduction zone. Bulletin of the Seismological Society of America, 100(1), 325–342. https://doi.org/10.1785/0120090156

Becker, D., Meier, T., Rische, M., Bohnhoff, M., & Harjes, H. P. (2006). Spatio-temporal microseismicity clustering in the Cretan region. Tectonophysics, 423(1–4), 3–16. https://doi.org/10.1016/j.tecto.2006.03.022

Becker, D., Meier, T., Bohnhoff, M., & Harjes, H. P. (2010). Seismicity at the convergent plate boundary offshore Crete, Greece, observed by an amphibian network. Journal of Seismology, 14(2), 369–392. https://doi.org/10.1007/s10950-009-9170-2

Benedetti, L., Finkel, R., Papanastassiou, D., King, G., Armijo, R., Ryerson, F., et al. (2002). Post-glacial slip history of the Sparta fault (Greece) determined by 36Cl cosmogenic dating: Evidence for non-periodic earthquakes. Geophysical Research Letters, 29(8), doi: 10.1029/2001GL014510. https://doi.org/10.1029/2001GL014510

Bohnhoff, M., Makris, J., Papanikolaou, D., & Stavrakakis, G. (2001). Crustal investigation of the Hellenic subduction zone using wide aperture seismic data. Tectonophysics, 343(3–4), 239–262. https://doi.org/10.1016/S0040-1951(01)00264-5

Bohnhoff, M., Harjes, H. P., & Meier, T. (2005). Deformation and stress regimes in the Hellenic subduction zone from focal mechanisms. Journal of Seismology, 9(3), 341–366. https://doi.org/10.1007/s10950-005-8720-5

Caputo, R., Monaco, C., & Tortorici, L. (2006). Multiseismic cycle deformation rates from Holocene normal fault scarps on Crete (Greece). Terra Nova, 18(3), 181–190. https://doi.org/10.1111/j.1365-3121.2006.00678.x

Caputo, R., Catalano, S., Monaco, C., Romagnoli, G., Tortorici, G., & Tortorici, L. (2010).

Active faulting on the island of Crete (Greece). Geophysical Journal International, 183(1), 111–126. https://doi.org/10.1111/j.1365-246X.2010.04749.x

Chaumillon, E., & Mascle, J. (1997). From foreland foreland to forearc forearc domains : domains : New New multichannel multichannel seismic reflection survey survey of of the the Mediterranean Mediterranean ridge ridge accretionary accretionary reflection complex. Marine Geology, 138(2), 237–259.

Cucci, L., D'Addezio, G., Valensise, G., & Burrato, P. (1996). Investigating seismogenic faults in Central and Southern Apennines (Italy): Modeling of fault-related landscape features. Annali Di Geofisica.

D'agostino, N., Cheloni, D., Fornaro, G., Giuliani, R., & Reale, D. (2012). Space-time distribution of afterslip following the 2009 L'Aquila earthquake. Journal of Geophysical Research: Solid Earth, 117(B2).

Devescovi, M., & Iveša, L. (2008). Colonization patterns of the date mussel Lithophaga lithophaga (L., 1758) on limestone breakwater boulders of a marina. Periodicum biologorum, 110(4), 339-345.

Doutsos, T., & Kokkalas, S. (2001). Stress and deformation patterns in the Aegean region. Journal of Structural Geology, 23(2–3), 455–472. https://doi.org/10.1016/S0191-8141(00)00119-X

Dziewonski, A. M., Chou, T. A., & Woodhouse, J. H. (1981). Determination of earthquake source parameters from waveform data for studies of global and regional seismicity. Journal of Geophysical Research: Solid Earth, 86(B4), 2825-2852.

Ekström, G., Nettles, M., & Dziewoński, A. M. (2012). The global CMT project 2004–2010: Centroid-moment tensors for 13,017 earthquakes. Physics of the Earth and Planetary Interiors, 200, 1-9.

Fassoulas, C. (2000). The tectonic development of a Neogene basin at the leading edge of the active European margin: The Heraklion basin, Crete, Greece. Journal of Geodynamics, 31(1), 49–70. https://doi.org/10.1016/S0264-3707(00)00017-X

Fassoulas, C., Kilias, A., & Mountrakis, D. (1994). Postnappe stacking extension and exhumation of high-pressure/low-temperature rocks in the island of Crete, Greece. Tectonics, 13(1), 127–138. https://doi.org/10.1029/93TC01955

Ferranti, L., Antonioli, F., Mauz, B., Amorosi, A., Dai Pra, G., Mastronuzzi, G., et al. (2006). Markers of the last interglacial sea-level high stand along the coast of Italy: Tectonic implications. Quaternary International, 145–146, 30–54. https://doi.org/10.1016/j.quaint.2005.07.009

Firth, C., & Stewart, I. (1996). Coastal elevation changes in eastern Sicily: implications for volcano instability at Mount Etna. Geological Society, …, (110), 153–167. https://doi.org/10.1144/GSL.SP.1996.110.01.12

Floyd, M. A., Billiris, H., Paradissis, D., Veis, G., Avallone, A., Briole, P., et al. (2010). A new velocity field for Greece: Implications for the kinematics and dynamics of the Aegean. Journal of Geophysical Research: Solid Earth, 115(10), 1–25. https://doi.org/10.1029/2009JB007040

Gaki-Papanastassiou, K., Maroukian, H., & Kourmpanian, V. (2011) The morphotectonic evolution of the southern half of Kythira Island (Ionian Sea, Greece). Geograficzne, P, 49–60.

Gaki-Papanastassiou, K., Karymbalis, E., Papanastassiou, D., & Maroukian, H. (2009). Quaternary marine terraces as indicators of neotectonic activity of the Ierapetra normal fault SE Crete (Greece). Geomorphology, 104(1–2), 38–46. https://doi.org/10.1016/j.geomorph.2008.05.037

Gallen, S. F., & Wegmann, K. W. (2016). River profile response to normal fault growth and linkage: An example from the Hellenic forearc of south-central Crete, Greece. Earth

Surface Dynamics, 5(1), 161–186. https://doi.org/10.5194/esurf-5-161-2017

Gallen, S. F., Wegmann, K. W., Bohnenstiehl, D. R., Pazzaglia, F. J., Brandon, M. T., & Fassoulas, C. (2014). Active simultaneous uplift and margin-normal extension in a forearc high, Crete, Greece. Earth and Planetary Science Letters, 398, 11–24. https://doi.org/10.1016/j.epsl.2014.04.038

Ganas, A., & Parsons, T. (2009). Three-dimensional model of hellenic arc deformation and origin of the cretan uplift. Journal of Geophysical Research: Solid Earth, 114(6), 1–14. https://doi.org/10.1029/2008JB005599

Ganas, A., Fassoulas, C., Moshou, A., Bozionelos, G., Papathanassiou, G., Tsimi, C., & Valkaniotis, S. (2017). Geological and seismological evidence for NW-SE crustal extension at the southern margin of Heraklion basin, Crete. Bulletin of the Geological Society of Greece, volume 51, pages 52-75. doi: http://dx.doi.org/10.12681/bgsg.15004

Houghton, S. L., Roberts, G. P., Papanikolaou, I. D., McArthur, J. M., & Gilmour, M. A. (2003). New 234U-230Th coral dates from the western Gulf of Corinth: Implications for extensional tectonics. Geophysical Research Letters, 30(19).

Howell, A., Jackson, J., Copley, A., McKenzie, D., & Nissen, E. (2017). Subduction and vertical coastal motions in the eastern Subduction and vertical coast motions in the eastern Mediterranean. Geophysical Journal International, (November), 593–620. https://doi.org/10.1093/gji/ggx307

Huguen, C., Mascle, J., Chaumillon, E., Woodside, J. M., Benkhelil, J., Kopf, A., & Volkonskaïa, A. (2001). Deformational styles of the eastern Mediterranean Ridge and surroundings from combined swath mapping and seismic reflection profiling. Tectonophysics, 343(1-2), 21-47.

International Seismological Centre, *On-line Bulletin*, http://www.isc.ac.uk, Internatl. Seismol. Cent., Thatcham, United Kingdom, 2016.

Ivy-Ochs, S., Schäfer, J., Kubik, P. W., Synal, H. A., & Schlüchter, C. (2004). Timing of deglaciation on the northern Alpine foreland (Switzerland). Eclogae Geologicae Helvetiae, 97(1), 47-55.

Jackson, J. A., & White, N. J. (1989). Normal faulting in the upper continental crust: observations from regions of active extension. Journal of Structural Geology, 11(1–2), 15–36. https://doi.org/10.1016/0191-8141(89)90033-3

Jackson, J. (1994). Active tectonics of the Aegean region. Annual Review of Earth and Planetary Sciences, 22(1), 239-271.

Jara-Muñoz, J., & Melnick, D. (2015). Unraveling sea-level variations and tectonic uplift in wave-built marine terraces, Santa María Island, Chile. Quaternary Research (United States), 83(1), 216–228. https://doi.org/10.1016/j.yqres.2014.10.002

Jara-Muñoz, J., Melnick, D., Zambrano, P., Rietbrock, A., González, J., Argandoña, B., & Strecker, M. R. (2017). Quantifying offshore fore-arc deformation and splay-fault slip using drowned Pleistocene shorelines, Arauco Bay, Chile. Journal of Geophysical Research: Solid Earth, 122(6), 4529–4558. https://doi.org/10.1002/2016JB013339

Kassaras, I., D. Kazantzidou-Firtinidou, A. Ganas, V. Kapetanidis, C. Tsimi, S. Valkaniotis, N. Sakellariou and S. Mourloukos, 2018. Seismic risk and loss assessment for Kalamata (SW Peloponnese, Greece) from neighbouring shallow sources. Bolletino di Geofisica Teorica e Applicata, Vol. 59, n.1, pp. 1-26

Kelletat, D., Kowalczyk, G., Schröder, B., & Winter, K. P. (1976). A synoptic view on the neotectonic development of the Peloponnesian coastal regions. *Zeitschrift der Deutschen Geologischen Gesellschaft*, 447-465.

Kelletat, D. (1991). The 1550 BP tectonic event in the Eastern Mediterranean as a basis for assessing the intensity of shore processes. *Zeitschrift für Geomorphologie*, 81, 181-194.

Kershaw, S., Guo, L., & Braga, J. C. (2005). A Holocene coral-algal reef at Mavra Litharia, Gulf of Corinth, Greece: Structure, history, and applications in relative sea-level change. Marine Geology, 215(3–4), 171–192. https://doi.org/10.1016/j.margeo.2004.12.003

Kokinou, E., & Kamberis, E. (2009). The structure of the Kythira-Antikythira strait, offshore SW Greece (35.7 -36.6 N). Geological Society, London, Special Publications, 311(May), 343–360. https://doi.org/10.1144/SP311.14

Kokinou, E., Tiago, A., & Evangelos, K. (2012). Structural decoupling in a convergent forearc setting (Southern Crete, Eastern Mediterranean). Bulletin of the Geological Society of America, 124(7–8), 1352–1364. https://doi.org/10.1130/B30492.1

Kreemer, C., & Chamot-Rooke, N. (2004). Contemporary kinematics of the southern Aegean and the Mediterranean Ridge. Geophysical Journal International, 157(3), 1377-1392.

Lambeck, K., & Chappell, J. (2001). Sea level change through the last glacial cycle. Science, 292(5517), 679-686.

Lajoie, K. R. (1986). Coastal tectonics. Active tectonics, 95-124.

Licciardi, J. M., Denoncourt, C. L., & Finkel, R. C. (2008). Cosmogenic36Cl production rates from Ca spallation in Iceland. Earth and Planetary Science Letters, 267(1–2), 365–377. https://doi.org/10.1016/j.epsl.2007.11.036

Lin, J., & Stein, R. S. (2004). Stress triggering in thrust and subduction earthquakes and stress interaction between the southern San Andreas and nearby thrust and strike-slip faults. Journal of Geophysical Research: Solid Earth, 109(B2), 1–19. https://doi.org/10.1029/2003JB002607

Makropoulos, K., Kaviris, G., & Kouskouna, V. (2012). An updated and extended earthquake catalogue for Greece and adjacent areas since 1900. Natural Hazards and Earth System Sciences, 12(5), 1425-1430.

Marrero, S. M., Phillips, F. M., Borchers, B., Lifton, N., Aumer, R., & Balco, G. (2016). Cosmogenic nuclide systematics and the CRONUScalc program. Quaternary

Geochronology, 31, 160–187. https://doi.org/10.1016/j.quageo.2015.09.005

Mascle, J., Le Quellec, P., Leite, O., & Jongsma, D. (1982). Structural sketch of the Hellenic continental margin between the western Peloponnesus and eastern Crete. Geology, 10(2), 113–116. https://doi.org/10.1130/0091-7613(1982)10<113:SSOTHC>2.0.CO;2

McClusky, S., Balassanian, S., Barka, A., Demir, C., Ergintav, S., Georgiev, I., et al. (2000). Global Positioning System constraints on plate kinematics and dynamics in the eastern Mediterranean and Caucasus. Journal of Geophysical Research, 105(B3), 5695. https://doi.org/10.1029/1999JB900351

McIntosh, K., Silver, E., & Shipley, T. (1993). Evidence and mechanisms for forearc extension at the accretionary Costa Rica Convergent Margin. Tectonics, 12(6), 1380–1392. https://doi.org/10.1029/93TC01792

McKenzie, D. (1978). Active tectonics of the Alpine—Himalayan belt: the Aegean Sea and surrounding regions. Geophysical Journal International, 55(1), 217-254.

McKenzie, D., & Jackson, J. (2012). Tsunami earthquake generation by the release of gravitational potential energy. Earth and Planetary Science Letters, 345, 1-8.

McNeill, L. C., & Collier, R. L. (2004). Uplift and slip rates of the eastern Eliki fault segment, Gulf of Corinth, Greece, inferred from Holocene and Pleistocene terraces. Journal of the Geological Society, 161(1), 81-92.

McNeill, L. C., Collier, R. E. L., De Martini, P. M., Pantosti, D., & D'Addezio, G. (2005). Recent history of the Eastern Eliki Fault, Gulf of Corinth: Geomorphology, palaeoseismology and impact on palaeoenvironments. Geophysical Journal International, 161(1), 154–166. https://doi.org/10.1111/j.1365-246X.2005.02559.x

Mildon, Z. K., Toda, S., Faure Walker, J. P., & Roberts, G. P. (2016). Evaluating models of Coulomb stress transfer: Is variable fault geometry important?. Geophysical Research Letters, 43(24).

Meier, T., Rische, M., Endrun, B., Vafidis, A., & Harjes, H. P. (2004). Seismicity of the Hellenic subduction zone in the area of western and central Crete observed by temporary local seismic networks. Tectonophysics, 383(3–4), 149–169. https://doi.org/10.1016/j.tecto.2004.02.004

Meier, T., Becker, D., Endrun, B., Rische, M., Bohnhoff, M., Stöckhert, B., & Harjes, H.-P. (2007). A model for the Hellenic subduction zone in the area of Crete based on seismological investigations. Geological Society, London, Special Publications, 291(1), 183–199. https://doi.org/10.1144/SP291.9

Mercier, J. L., Sorel, D., & Simeakis, K. (1987). Changes in the state of stress in the overriding plate of a subduction zone: the Aegean Arc from the Pliocene to the Present. Annales tectonicae,1 (1) 20-39.

Meschis, M., Roberts, G. P., Robertson, J., & Briant, R. M. (2018). The Relationships Between Regional Quaternary Uplift, Deformation Across Active Normal Faults, and Historical Seismicity in the Upper Plate of Subduction Zones: The Capo D'Orlando Fault, NE Sicily. Tectonics, 1–25. https://doi.org/10.1029/2017TC004705

Meulenkamp, J. E., van der Zwaan, G. J., & van Wamel, W. A. (1994). On late miocene to recent vertical motions in the Cretan segment of the Hellenic arc. Tectonophysics, 234(1–2), 53–72. https://doi.org/10.1016/0040-1951(94)90204-6

Michetti, A. M., Ferreli, L., Serva, L., & Vittori, E. (1997). Geological evidence for strong historical earthquakes in an "aseismic" region: The Pollino case (southern Italy). Journal of Geodynamics, 24(1-4), 67-86.

Michetti, A. M., Ferreli, L., Esposito, E., Porfido, S., Blumetti, A. M., Vittori, E., et al. (2000). Ground Effects during the 9 September 1998, Mw = 5.6 Lauria Earthquake and the Seismic Potential of the "Aseismic" Pollino Region in Southern Italy. Seismological Research Letters, 71(1), 31–46. https://doi.org/10.1785/gssrl.71.1.31

Miller, W. R., & Mason, T. R. (1994). Erosional Features of Coastal Beachrock and Aeolianite Outcrops in Natal and Zululand, South Africa. Journal of Coastal Research, 10(2), 374–394. https://doi.org/10.2307/4298223

Monaco, C., & Tortorici, L. (2004). Faulting and effects of earthquakes on Minoan archaeological sites in Crete (Greece). Tectonophysics, 382(1–2), 103–116. https://doi.org/10.1016/j.tecto.2003.12.006

Morewood, N. C., & Roberts, G. P. (1999). Lateral propagation of the surface trace of the South Alkyonides normal fault segment, central Greece: Its impact on models of fault growth and displacement-length relationships. Journal of Structural Geology, 21(6), 635–652. https://doi.org/10.1016/S0191-8141(99)00049-8

Mouslopoulou, V., Nicol, A., Begg, J., Oncken, O., & Moreno, M. (2015a). Clusters of megaearthquakes on upper plate faults control the Eastern Mediterranean hazard. Geophysical Research Letters, 42(23), 10282–10289. https://doi.org/10.1002/2015GL066371

Mouslopoulou, V., Begg, J., Nicol, A., Oncken, O., & Prior, C. (2015b). Formation of Late Quaternary paleoshorelines in Crete, Eastern Mediterranean. Earth and Planetary Science Letters, 431, 294–307. https://doi.org/10.1016/j.epsl.2015.09.007

Mouslopoulou, V., Begg, J., Fülling, A., Moraetis, D., Partsinevelos, P., & Oncken, O. (2017). Distinct phases of eustatic and tectonic forcing for late Quaternary landscape evolution in southwest Crete, Greece. Earth Surface Dynamics, 5(3), 511–527. https://doi.org/10.5194/esurf-5-511-2017

National Observatory of Athens, Institute of Geodynamics, Athens (1997): National Observatory of Athens Seismic Network. International Federation of Digital Seismograph Networks. Other/Seismic Network. 10.7914/SN/HL

Nocquet, J. M. (2012). Present-day kinematics of the Mediterranean: A comprehensive overview of GPS results. Tectonophysics, 579, 220–242. https://doi.org/10.1016/j.tecto.2012.03.037

Ozawa, S., Nishimura, T., Suito, H., Kobayashi, T., Tobita, M., & Imakiire, T. (2011). Coseismic and postseismic slip of the 2011 magnitude-9 Tohoku-Oki earthquake. Nature, 475(7356), 373.

Palumbo, L., Benedetti, L., Bourlès, D., Cinque, A., & Finkel, R. (2004). Slip history of the Magnola fault (Apennines, Central Italy) from 36Cl surface exposure dating: Evidence for strong earthquakes over the Holocene. Earth and Planetary Science Letters, 225(1–2), 163–176. https://doi.org/10.1016/j.epsl.2004.06.012

Papadimitriou, E. E., & Karakostas, V. G. (2008). Rupture model of the great AD 365 Crete earthquake in the southwestern part of the Hellenic Arc. Acta Geophysica, 56(2), 293–312. https://doi.org/10.2478/s11600-008-0001-6

Papanikolaou, D., & Vassilakis, E. (2010). Thrust faults and extensional detachment faults in Cretan tectono-stratigraphy: Implications for Middle Miocene extension. Tectonophysics, 488(1–4), 233–247. https://doi.org/10.1016/j.tecto.2009.06.024

Papanikolaou, D., Fountoulis, I., & Metaxas, C. (2007). Active faults, deformation rates and Quaternary paleogeography at Kyparissiakos Gulf (SW Greece) deduced from onshore and offshore data. Quaternary International, 171–172(SPEC. ISS.), 14–30. https://doi.org/10.1016/j.quaint.2007.04.005

Papanikolaou, I. D., Foumelis, M., Parcharidis, I., Lekkas, E. L., & Fountoulis, I. G. (2010). Deformation pattern of the 6 and 7 April 2009, MW= 6.3 and MW= 5.6 earthquakes in L'Aquila (Central Italy) revealed by ground and space based observations. Natural Hazards and Earth System Sciences, 10(1), 73.

Papanikolaou, I. D., & Roberts, G. P. (2007). Geometry, kinematics and deformation rates along the active normal fault system in the southern Apennines: Implications for fault growth. Journal of Structural Geology, 29(1), 166–188. https://doi.org/10.1016/j.jsg.2006.07.009

Papazachos, B. C. (1990). Seismicity of the Aegean and surrounding area. Tectonophysics, 178(2–4), 287–308. https://doi.org/10.1016/0040-1951(90)90155-2

Papazachos, B. C., Papadimitriou, E. E., Kiratzi, A. A., Papazachos, C. B., & Louvari, E. K. (1998). Fault plane solutions in the Aegean Sea and the surrounding area and their tectonic implications. Boll. Geof. teor. appl, 39(3), 199-218.

Papoulia, J., & Makris, J. (2004). Microseismicity and active deformation of Messinia, SW Greece. Journal of Seismology, 8(4), 439–451. https://doi.org/10.1007/s10950-004-4837-1

Papoulia, J., Nicolich, R., Makris, J., Slejko, D., Mascle, J., Papadopoulos, G., et al. (2014). A new seismogenic model for the Kyparissiakos Gulf and western Peloponnese (SW Hellenic Arc). Bollettino Di Geofisica Teorica Ed Applicata, 55(2), 405–432. https://doi.org/10.4430/bgta0127

Pedoja, K., Husson, L., Johnson, M. E., Melnick, D., Witt, C., Pochat, S., et al. (2014). Coastal staircase sequences reflecting sea-level oscillations and tectonic uplift during the Quaternary and Neogene. Earth-Science Reviews, 132, 13–38. https://doi.org/10.1016/j.earscirev.2014.01.007

Pedoja, K., Jara-Muñoz, J., De Gelder, G., Robertson, J., Meschis, M., Fernandez-Blanco, D., et al. (2017). Neogene-Quaternary slow coastal uplift of Western Europe through the per- spective of sequences of strandlines from the Cotentin Peninsula (Normandy, France). Geomorphology. https://doi.org/10.1016/j.geomorph.2017.11.021

Peharda, M., Puljas, S., Chauvaud, L., Schöne, B. R., Ezgeta-Balić, D., & Thébault, J. (2015). Growth and longevity of Lithophaga lithophaga: what can we learn from shell structure and stable isotope composition?. Marine biology, 162(8), 1531-1540.

Peterek, A., & Schwarze, J. (2004). Architecture and Late Pliocene to recent evolution of outer-arc basins of the Hellenic subduction zone(south-central Crete, Greece). Journal of Geodynamics, 38(1), 19–55. https://doi.org/10.1016/j.jog.2004.03.002

Pichon, X. Le, & Angelier, J. (1979). The hellenic arc and trench system: A key to the neotectonic evolution of the eastern mediterranean area. Tectonophysics, 60(1–2), 1–42. https://doi.org/10.1016/0040-1951(79)90131-8

Pirazzoli, P. A., Thommeret, J., Thommeret, Y., Laborel, J., & Montag-Gioni, L. F. (1982). Crustal block movements from Holocene shorelines: Crete and Antikythira (Greece). Tectonophysics, 86(1-3), 27-43.

Pirazzoli, P. A., Laborel, J., & Stiros, S. C. C. (1996). Earthquake clustering in the Eastern Mediterranean during historical times. Journal of Geophysical Research, 101(B3), 6083–6097. https://doi.org/10.1029/95JB00914

Postma, G., & Nemec, W. (1990). Regressive and transgressive sequences in a raised Holocene gravelly beach, southwestern Crete. Sedimentology, 37(5), 907–920. https://doi.org/10.1111/j.1365-3091.1990.tb01833.x

Reimer, P., Bard, E., Bayliss, A., Beck, J., Blackwell, P., Ramsey, C., et al. (2013). Intcal13 and marine13 radiocarbon age calibration curves 0 – 50,000 years cal bp. Radiocarbon, 55(4), 1869–1887. https://doi.org/10.2458/rc.v51i4.3569

Roberts, G. P. (1996). Variation in fault-slip directions along active and segmented normal fault systems. Journal of Structural Geology, 18(6), 835–845. https://doi.org/10.1016/S0191-8141(96)80016-2

Roberts, G. P. (2007). Fault orientation variations along the strike of active normal fault systems in Italy and Greece: Implications for predicting the orientations of subseismic-resolution faults in hydrocarbon reservoirs. AAPG Bulletin, 91(1), 1–20. https://doi.org/10.1306/08300605146

Roberts, G. P., & Ganas, A. (2000). Fault-slip directions in central and southern Greece measured from striated and corrugated fault planes: Comparison with focal mechanism and geodetic data. Journal of Geophysical Research, 105(1999), 23443. https://doi.org/10.1029/1999JB900440

Roberts, G. P., & Michetti, A. M. (2004). Spatial and temporal variations in growth rates along active normal fault systems: An example from The Lazio-Abruzzo Apennines, central Italy. Journal of Structural Geology, 26(2), 339–376. https://doi.org/10.1016/S0191-8141(03)00103-2

Roberts, G. P., Houghton, S. L., Underwood, C., Papanikolaou, I., Cowie, P. A., Van Calsteren, P., et al. (2009). Localization of quaternary slip rates in an active rift in 105 years: An example from central Greece constrained by 234U- 230Th coral dates from uplifted paleoshorelines. Journal of Geophysical Research: Solid Earth, 114(10), 1–26. https://doi.org/10.1029/2008JB005818

Roberts, G. P., Meschis, M., Houghton, S., Underwood, C., & Briant, R. M. (2013). The implications of revised Quaternary palaeoshoreline chronologies for the rates of active extension and uplift in the upper plate of subduction zones. Quaternary Science Reviews, 78, 169–187. https://doi.org/10.1016/j.quascirev.2013.08.006

Rohling, E. J., Foster, G. L., Grant, K. M., Marino, G., Roberts, A. P., Tamisiea, M. E., & Williams, F. (2014). Sea-level and deep-sea-temperature variability over the past 5.3 million years. Nature, 508(7497), 477–482. https://doi.org/10.1038/nature13230

Saillard, M., Hall, S. R., Audin, L., Farber, D. L., Regard, V., & Hérail, G. (2011). Andean coastal uplift and active tectonics in southern Peru:10Be surface exposure dating of differentially uplifted marine terrace sequences (San Juan de Marcona, ~15.4°S). Geomorphology, 128(3–4), 178–190. https://doi.org/10.1016/j.geomorph.2011.01.004

Sak, P. B., Fisher, D. M., Gardner, T. W., Marshall, J. S., & LaFemina, P. C. (2009). Rough crust subduction, forearc kinematics, and Quaternary uplift rates, Costa Rican segment of the Middle American Trench. Bulletin of the Geological Society of America, 121(7–8), 992–1012. https://doi.org/10.1130/B26237.1

Schimmelpfennig, I., Benedetti, L., Finkel, R., Pik, R., Blard, P. H., Bourlès, D., et al. (2009). Sources of in-situ 36Cl in basaltic rocks. Implications for calibration of production rates. Quaternary Geochronology, 4(6), 441–461. https://doi.org/10.1016/j.quageo.2009.06.003

Schlagenhauf, A., Gaudemer, Y., Benedetti, L., Manighetti, I., Palumbo, L., Schimmelpfennig, I., et al. (2010). Using in situ Chlorine-36 cosmonuclide to recover past earthquake histories on limestone normal fault scarps: A reappraisal of methodology and interpretations. Geophysical Journal International, 182(1), 36–72. https://doi.org/10.1111/j.1365-246X.2010.04622.x

Shakun, J. D., Lea, D. W., Lisiecki, L. E., & Raymo, M. E. (2015). An 800-kyr record of global surface ocean δ18O and implications for ice volume-temperature coupling. Earth and Planetary Science Letters, 426, 58-68.

Shaw, B. (2012). Active tectonics of the Hellenic subduction zone, 7–29. https://doi.org/10.1007/978-3-642-20804-1

Shaw, B., & Jackson, J. (2010). Earthquake mechanisms and active tectonics of the Hellenic subduction zone. Geophysical Journal International, 181(2), 966–984. https://doi.org/10.1111/j.1365-246X.2010.04551.x

Shaw, B., Ambraseys, N. N., England, P. C., Floyd, M. A., Gorman, G. J., Higham, T. F. G., et al. (2008). Eastern Mediterranean tectonics and tsunami hazard inferred from the AD 365 earthquake. Nature Geoscience, 1(4), 268–276. https://doi.org/10.1038/ngeo151

Siddall, M., Rohling, E., Almogi-Labin, a, Hemleben, C., Meischner, D., Schmelzer, I., & Smeed, D. a. (2003). Sea-level fluctuations during the last glacial cycle. Nature, 423(June), 853–858. https://doi.org/10.1038/nature01687.1.

Skourtsos, E., Pope, R., & Triantaphylleou, M. V. (2007). Tectono-Sedimentary Evolution and Rates of Tectonic Uplift of the Sfakia Coastal Zone, Southwestern Crete. Bulletin of the Geological Society of Greece: Proceedings of the 11th International Congress, XXXVII(1), 475–487. https://doi.org/10.1111/j.1365-2699.2009.02106.x

Snopek, K., Meier, T., Endrun, B., Bohnhoff, M., & Casten, U. (2007). Comparison of gravimetric and seismic constraints on the structure of the Aegean lithosphere in the forearc of the Hellenic subduction zone in the area of Crete. Journal of Geodynamics, 44(3–5), 173–185. https://doi.org/10.1016/j.jog.2007.03.005

Spratt, R. M., & Lisiecki, L. E. (2016). A Late Pleistocene sea level stack. Climate of the Past, 12(4), 1079-1092.

Stiros, S. C. (2001). The AD 365 Cret earthquake and possible seismic clustering during the fourth to sixth centuries AD in the Eastern Mediterranean: A review of historical and archaeological data. Journal of Structural Geology, 23(2–3), 545–562. https://doi.org/10.1016/S0191-8141(00)00118-8

Stiros, S. C. (2010). The 8.5+ magnitude, AD365 earthquake in Crete: Coastal uplift, topography changes, archaeological and historical signature. Quaternary International, 216(1–2), 54–63. https://doi.org/10.1016/j.quaint.2009.05.005

Stone, J., Lambeck, K., Fifield, L. K., Evans, J. M., & Cresswell, R. G. (1996). A Lateglacial age for the Main Rock Platform, western Scotland. Geology, 24(8), 707–710. https://doi.org/10.1130/0091-7613(1996)024<0707:ALAFTM>2.3.CO;2

Strasser, T. F., Runnels, C., Wegmann, K., Panagopoulou, E., Mccoy, F., Digregorio, C., et al. (2011). Dating Palaeolithic sites in southwestern Crete, Greece. Journal of Quaternary Science, 26(5), 553–560. https://doi.org/10.1002/jqs.1482

Strobl, M., Hetzel, R., Fassoulas, C., & Kubik, P. W. (2014). A long-term rock uplift rate for eastern Crete and geodynamic implications for the Hellenic subduction zone. Journal of Geodynamics, 78, 21–31. https://doi.org/10.1016/j.jog.2014.04.002

Subarya, C., Chlieh, M., Prawirodirdjo, L., Avouac, J. P., Bock, Y., Sieh, K., ... & McCaffrey, R. (2006). Plate-boundary deformation associated with the great Sumatra–Andaman earthquake. Nature, 440(7080), 46.

Taymaz, T., Jackson, J., & Westaway, R. (1990). Earthquake mechanisms in the Hellenic Trench near Crete. Geophysical Journal International, 102(3), 695–731. https://doi.org/10.1111/j.1365-246X.1990.tb04590.x

Ten Veen, J. H., & Meijer, P. T. (1998). Late Miocene to Recent tectonic evolution of Crete (Greece): geological observations and model analysis. *Tectonophysics*, 298(1-3), 191-208.

Ten Veen, J. H,, & Kleinspehn, K. L. (2003). Incipient continental collision and plate-boundary curvature: Late Pliocene–Holocene transtensional Hellenic forearc, Crete, Greece. J*ournal of the Geological Society*, 160(2), 161-181.

Tiberti, M. M., Basili, R., & Vannoli, P. (2014). Ups and downs in western Crete (Hellenic subduction zone). Scientific Reports, 4, 5677. https://doi.org/10.1038/srep05677

Toda, S., Stein, R. S., Richards-Dinger, K., & Bozkurt, S. B. (2005). Forecasting the evolution of seismicity in southern California: Animations built on earthquake stress transfer. Journal of Geophysical Research: Solid Earth, 110(5), 1–17. https://doi.org/10.1029/2004JB003415

Tortorici, G., Bianca, M., de Guidi, G., Monaco, C., & Tortorici, L. (2003). Fault activity and marine terracing in the Capo Vaticano area (southern Calabria) during the Middle-Late Quaternary. Quaternary International, 101–102(1), 269–278. https://doi.org/10.1016/S1040-6182(02)00107-6

Tsimi, C., Ganas, A., Ferrier, G., Drakatos, G., Pope, R. J., & Fassoulas, C. (2007).

Morphotectonics of the Sfakia normal fault, southwestern Crete, Greece. Proceedings of 8th Pan-Hellenic Geographical Conference, volume 1 (186-194), 4 - 7 October 2007, Athens (Greece)

van Hinsbergen, D. J., & Meulenkamp, J. E. (2006). Neogene supra detachment basin development on Crete (Greece) during exhumation of the South Aegean core complex. Basin Research, 18(1), 103-124.

Vigny, C., Socquet, A., Peyrat, S., Ruegg, J. C., Métois, M., Madariaga, R., ... & Carrizo, D. (2011). The 2010 Mw 8.8 Maule megathrust earthquake of central Chile, monitored by GPS. Science, 332(6036), 1417-1421.

Waelbroeck, C., Labeyrie, L., Michel, E., Duplessy, J. C., McManus, J. F., Lambeck, K., ... & Labracherie, M. (2002). Sea-level and deep water temperature changes derived from benthic foraminifera isotopic records. Quaternary Science Reviews, 21(1-3), 295-305.

Walsh, J. J., Nicol, A., & Childs, C. (2002). An alternative model for the growth of faults. Journal of Structural Geology, 24(11), 1669-1675.

Wardell, N., Camera, L., Mascle, J., Nicolich, R., Marchi, M., & Barison, E. (2014). The structural framework of the Peloponnese continental margin from Zakynthos to Pylos from seismic reflection and morpho-bathymetric data. Bollettino Di Geofisica Teorica Ed Applicata, 55(2), 343–367. https://doi.org/10.4430/bgta0087

Wells, D. L., & Coppersmith, K. J. (1994). New Empirical Relationships among Magnitude, Rupture Length, Rupture Width, Rupture Area, and Surface Displacement. Bulletin of the Seismological Society of America, 84(4), 974–1002. https://doi.org/<p></p>

Westaway, R. (1993). Quaternary uplift of southern Italy. Journal of Geophysical Research, 98(B12), 741–772. https://doi.org/10.1029/93JB01566

Wilkinson, M., Roberts, G. P., McCaffrey, K., Cowie, P. A., Faure Walker, J. P., Papanikolaou, I., et al. (2015). Slip distributions on active normal faults measured from

LiDAR and field mapping of geomorphic offsets: An example from L'Aquila, Italy, and implications for modelling seismic moment release. Geomorphology, 237, 130–141. https://doi.org/10.1016/j.geomorph.2014.04.026

Zygouri, V., Koukouvelas, I., & Ganas, A. (2016). Palaeoseismological Analysis of the East Giouchtas Fault, Heraklion Basin, Crete (Prelimenary Results). *Bulletin of the Geological Society of Greece*, 50(1), 563-571.

Sample reference	Profile reference	Latitude (°)	Longitude (°)	Elevation (m)	Inner-edge Elevation (m)	Erosion rate (mm/kyr)	Total erosion (mm)	Cl (p.p.m)	±	^{36}Cl (g of rock)	±	CaO (wt%)	±	Age (kyr)	Internal uncertainty (kyr)	Total uncertainty (kyr)
S1	Profile 10	34.98335	25.3472	43	54	0.1	13.4	26.7499	0.626047	2137936	74973	50.8388	1.17	134	0.92	33
S2	Profile 4	34.98417	25.282	20	38	0.1	4	40.54	1.191038	677147	21952	49.4534	1.21	40	0.22	7.5
S3	Profile 4	34.98303	25.2788	34	38	0.1	6.1	41.0464	1.200486	1027505	33320	49.584	1.28	61	0.4	13
S4	Profile 5	34.98106	25.2782	65	67	0.1	8.8	29.4929	0.720745	1464291	44509	50.1486	1.14	88	0.52	21
S5	Profile 5	34.98207	25.2785	80	116	0.1	10.8	33.0023	0.868346	1770564	53271	48.5666	1.21	108	0.66	24

Table 1: ^{36}Cl data for all samples

				Measured palaeoshoreline elevations (this study)		Siddall et al 2003/Rohling et al 2014					
Profile reference	Uplift (mm/yr)	UTM of altimeter msmts Easting	Northing	DEM palaeoshoreline elevations (this study) (m)	Barometric altimeter palaeoshoreline elevations (this study) (m)	Allocated highstand age (ka)	Predicted palaeoshoreline elevations (m) (Siddall et al, 2003)	RMSD	Profile reference (Gallen et al., 2014)	Allocated highstand age (ka)	Measured palaeoshoreline elevations (Gallen et al., 2014) (m)
1	0.58 ± 0.09					76.5	14	9.01	7	78	13
				34		100	33				
				71		125	78				
				277		478	277				
				439		740	439				
				584		980	584				
2	0.72 ± 0.10			26		76.5	25	4.71	8	78	**25**
										82	43
						100	47			107	60
				97		125	95			123	96
				139		200	139				
				174		285	175				
				395		525	395				
				534		740	538				
3	0.75 ± 0.08					76.5	27	7.75	9	78	30
										82	47
				51		100	50			107	65
				98		125	99			123	103
				185		285	184				
				566		740	560				
				651		855	661				
4	0.89 ± 0.09			38		76.5	38	7.63	10	72	**27**
										82	43
		342710	3872265	**68**	67	100	64			107	62
				116		125	116			123	97
						200	173			215	140
				211		240	209				
						285	224			287	166
				310		340	308			330	210
						410	360			405	251
				482		525	487				
				506		560	501				
5	0.88 ± 0.08	342882	3872461	38	**38**	76.5	38	12.56			
				57		100	62				
				201		240	204				
				258		310	248				
				304		340	301				
				415		478	416				
				497		560	490				
6	0.39 ± 0.09			55		125	55	4.55	11	123	50
						200	75			215	65
				86		240	91				
				105		340	102			330	103
7	0.38 ± 0.09			50		125	53	2.7			
		345779	3873003	72	74	200	71				
		345763	3873855	134	136	340	134				
8	0.39 ± 0.08			53		125	53	4.23			
				72		200	71				
				88		240	86				
				138		340	134				
				146		410	151				
9	0.38 ± 0.11	347082	3873046	11	12	100	12	3.04	12		
				51		125	51			123	**50**
						200	69			215	70
				86		240	84				
						340	131			330	105
				149		410	147				
10	0.37 ± 0.09	349877	3873397	52	**54**	125	51	3.65			
				67		200	69				
				83		240	84				
				99		310	93				
11	0.29 ± 0.06			53		200	55	2.92			
		352204	3874596		69	240	67				
		352238	3874670	104	105	340	107				
12	0.3 ± 0.08	353581	3874152		41	125	43	2.12	13	123	42
						200	55			215	55
		353707	3874364	69	70	240	67				
		353789	3874574	106	105	340	105			330	92
13	0.3 ±0.07	356636	3873273	45	45	125	45	6.52	14*	123	45
		356352	3873458	55	56	200	55			215	61
		355492	3873344	67	68	240	67				
				102		340	107			330	114
				120		410	118				
14	0.29 ± 0.08	358624	3873366	40	41	125	40	6.42	15	123	1
		358618	3873493	53	53	200	51			215	39
				69		240	62				
				94		340	100			330	50
15	0.28 ± 0.08			43		125	40	4.9			
				54		200	51				
				60		240	62				
				98		340	100				
16	0.25 ± 0.08	360348	3873126		38	125	36	1.84			
		359983	3873325	57	55	240	55				
				91		340	90				
17	0.24 ± 0.09			33		125	35	6.72	16**	123	2
						200	43			215	40
		361216	3872978	55	56	240	53				
		361280	3873130		85	340	87			330	59
				99		410	93				

* Location of my profile is 130 m to the east of Gallen's location
** Location of my profile is 220 m to the west of Gallen's location

Table 2: Calculator data for all profiles

Uplift (mm/yr)	R^2	RMSE	UTM of altimeter msmts		Allocated highstand age (ka)	Predicted palaeoshoreline elevations (m)	DEM palaeoshoreline elevations (this study) (m)	Barometric altimeter palaeoshoreline elevations (this study)
			Easting	Northing				
0.71 ± 0.02	0.9982	7.16	358496	3874675	478	339	336	336
			358995	3874892	525	393	395	394
			358840	3874889	550	401	405	406
					560	401		
					590	439	440	
					620	460	462	
					695	503	504	

Table 3: Footwall calculator data for Profile 14 footwall profile.

Fault name	Fault information (fault trace, kinematics)	Length (km)	Depth of seismogenic zone (km)	Dip °	Dip direction °	Rake °	Sub-surface slip value (m)	Max. Mw
Ptolemy trench	Kokinou et al., 2012; Becker at al 2006, 2009; Meier et al., 2004, Ozbakir et al., 2013	94	30	85	150	-40	4.3	7.3
Offshore normal faults:	Kokinou et al., 2012; Mascle 1982; Caputo et al., 2010; Gallen et al., 2014							
Fault 1 (aka. Lithino fault)		14.8	15	60	180	-90	0.75	6.1
Fault 2 (aka. Lithino fault)		18.2	15	60	180	-90	1	6.2
Fault 3 (aka. Mirto fault)		13	15	60	170	-90	0.6	6
Fault 4 (aka. Mirto fault		19	15	60	170	-90	1	6.2
Fault 3&4 combined (aka. Mirtos fault)		37	15	60	155	-90	2.2	6.7

Table 4: Coulomb input data. Slip at the surface is set at 0.1 (10%) of the slip value at depth. This is based upon the relationship between surface slip (Vittori et al., 2011) and maximum slip values at depth (Wilkinson et al., 2015) for the Mw 6.3 2009 L'Aquila earthquake. The seismogenic layer depth is considered to be 15 km, with the exception of the Ptolemy fault which has been imaged to 30 km by Meier et al., 2004

Captions

Figure 1

(a)Tectonic setting of Crete, Greece. GPS data is from Nocquet et al., 2012. The location of the Hellenic subduction zone is taken from Kreemer and Chamot-Rooke, 2004. Dots show earthquakes between 1900-2009 >Mw 4, constrained to a depth ≤30 km (Makropoulos et al., 2012); fault plane solutions for earthquakes constrained to a depth ≤30 between 1953-1995 (Mw ≥5.5) (Papazachos et al., 1998) and 1995-2018 (Mw 4) (CMT Catalog: Dziewonski et al., 1981; Ekstrom et al., 2012). (b) Velocity field for Greece (Nocquet et al., 2012) (c) map of Crete with possible active arc-normal upper-plate faults labelled: Ka: Kastelli fault (Caputo et al., 2010); Sf: Sfakia (Caputo et al., 2010); Se/A: Sellia/Asomatos (Caputo et al., 2010); Sp: Spilli (Monaco and Tortorici, 2004); Caputo et al., 2010); AgG: Agia Galini (Monaco and Tortorici, 2004; Caputo et al 2010); Ier: Ierapetra (Caputo et al., 2010); Ms: Messara (Fassoulas, 2001); CL: Cape Lithino (Caputo et al., 2010); Mr: Mirto (Caputo et al., 2010) SCCF: South Central Crete Fault (Gallen et al., 2014); Pt: Ptolemy trench fault (Mascle et al., 1982; Becker et al., 2006, 2009; Kokinou et al., 2012).

Figure 2

5 m Digital Elevation Models of (a) the research area and (b-e) detailed views of the DEMs. Locality names and annotations can be found within Figure 3.

Figure 3

5 m Digital Elevation Models: (a) location of topographic profiles (numbered). Observed fault location from fieldwork during 2015 and 2016; inferred fault location is obtained from IGME Ano Viannos 1:50,000 map. Locations of figures (b), (c) and (e) are shown by dashed boxes in (a). (b) western section of the study area from Profile 1 (Agios Ioannis) to Profile 5 (Tsoutsouros), inset location is shown in detail in (d). (c) eastern study area from Profile 6 (Tsoutsouros) to Profile 10 (Kastri). (d) detailed view of west of Tsoutsouros Bay (TB). (e) eastern study area from Profile 11 (Kastri) to profile 17 (Arvi). Dating locations using ^{36}Cl (this study) and OSL (Gallen et al., 2014) are shown. Locations of photographs featured in (Fig.7) are marked.

Figure 4

Overview of the method used for allocating highstand ages to inner-edge elevations for each topographic profile, illustrated used Profile 10. (a) Topographic profile 10 with an uplift rate of 0.37 mm/yr. Horizontal coloured lines show the predicted elevations of highstands obtained using the Terrace Calculator, which shows some older highstands overprinted by younger highstands, this is clear in (c). Tie points between observed (field or DEM) inner edges and those predicted are marked. Initial uplift value is derived from the dated ^{36}Cl sample S1 (b) Terrace calculator data for topographic profile 10. (c) Predicted highstand elevations for topographic Profile 10, graph shows the highstands which would not be preserved (black squares) given the 0.37 mm/yr uplift rate (d) RMSE values for all uplift scenarios from 0 to 1 mm/yr at intervals of 0.05 mm/yr when the 125 ka highstand is tied to the 54 m palaeoshoreline.

Figure 5:

Schematic cartoon of the features commonly observed on palaeoshorelines and the associated wave-cut platforms.

Figure 6:

^{36}Cl exposure dating location photographs and cross section illustrations showing palaeogeological evidence for sample locations S1 (a-c), S2 (d and h), S3 (d and g), S4 (d and i), and S5 (d, e-f). Inner edges are marked by arrows on (d).

Figure 7:

Field photographs (see Figure 3 for locations). (a) Photograph of hangingwall terraces cut into Miocene sediments against the limestone fault scarp and footwall, (ai) shows a close up of the slot gorge near to Arvi (Figure 3, profile 14) with visible bedrock scarps identified by red arrows. (b) overview of the profile 4 and 5 area and the locations of ^{36}Cl samples S2 S3, S4 and S5. Arrows show the palaeoshorelines of the 76.5, 100 and 125 ka highstands. (c) Profile 4, lower terrace (76.5 ka). Lithophagid borings are visible on the limestone outer edge (h) and palaeostep (g) at 27 m. (d) Detailed view of the S4 sample site at 60 m on profile 4; lithophagid borings in limestone are clear and remains of a serpulid algal reef surround part of the limestone. (e) Profile 10 at 43 m contact between algal serpulid reef and beach conglomerate both deposited during the 125 ka highstand allocated to this elevation. (f) Overview Profile 10 palaeoshoreline at 54 m and associated wave-cut platform, ^{36}Cl sample S1 was removed from this location. (g) and (h) lithophagid borings along profile 4 (i) Profile 10 at 43 m, an eroded millhole cut into limestone within 1 m of the sampling location for S1.

Figure 8:

(a) ^{36}Cl sample ages and associated errors. (b) ages and errors plotted onto the Siddall et al. (2003) sea-level curve, the two lines represent two cores used in their study. (c) Preferred uplift scenario of 0.89 achieved by tying S3 to the 76.5 ka highstand. Note that while only the allocation to highstands 76.5, 100 and 125 ka are shown in (c), matches between measured inner-edge elevations and predicted inner-edge elevations up to 980 ka were carried out (detailed in Supplementary Figure 2, Supplementary Table 2). Predicted vs matched elevations were evaluated using R^2.

Figure 9:

Topographic profiles for all profile lines which run perpendicular to the strike of the faults (see Figure 3b for locations of profile lines), obtained from 5 m DEMs. Measured (DEM or field) elevations of inner-edges are matched against highstand elevations predicted by the Terrace Calculator given an iterated uplift value (see Figure 4 for further explanation). Locations of ^{36}Cl dated samples (this study) and OSL dated samples (Gallen et al., 2014) are shown alongside the ages obtained. Detailed topographic profiles are shown for 0-400 m for profiles 5 (f) and 4 (e). See text for an explanation of along strike correlation between palaeoshorelines. Figures (a-g) show profiles in the footwall of an offshore fault; figures (h-s) are in the hangingwall of the SCCF onshore fault.

Figure 10:

Measured (DEM and field) versus predicted palaeoshoreline elevations from the Terrace Calculator, error values are small and contained within the size of the symbols which represent each data point.

Figure 11:

(a-p) Elevation of measured inner-edge elevations plotted against highstand age for each topographic profile, error values are small and contained within the size of the symbols which represent each data point.

Figure 12:

(a) Along-strike palaeoshoreline elevations for the footwall and hangingwall terraces from profile 1 in the west to profile 17 in the east (see Figure 3a for locations). Vertical dotted line indicates point at which the curving SCCF fault trace is crossed. (b) location of the offshore Ptolemy fault and the onshore SCCF with dating locations (this study and Gallen et al., 2014) also marked.

Figure 13:

(a) Footwall uplift along strike (Profile 1 - 5). (b) Hangingwall uplift along strike (Profile 6 - 17). (c) Tilt angles of FW terraces from profiles 1 - 4 (tip to the highest point of the fault). (d) Tilt angles of HW terraces from profiles 6 - 17 (tip to the lowest point of the fault) (see Supplementary Figure 5 for actual tilt values).

Figure 14:

Coulomb models of the vertical deformation (m) caused by offshore upper-plate faults as a result of a standard earthquake (see Table 4 for input values). Crete coastline is outlined in black with the profile lines (numbered every alternate profile; blue lines are faults; green lines represent the faults modelled; contours represent uplift (red) and subsidence (blue) at the surface. (a) modelling only the Ptolemy fault results in a maximum value of 0.4 m of coseismic uplift at profile 2 where the 76.5 ka palaeoshoreline is at 25 m (Table 2); (b) modelling the offshore normal Cape Lithino and Mirto faults (see table 4 for input values) results in 0.01-0.02 m of coseismic uplift at profile 2 where the 76.5 ka palaeoshoreline is at 25 m (Table 2). Tests to obtain the recurrence intervals for the 25 m, 76.5 ka palaeoshoreline at profile 2 are shown in (c) for coseismic uplift along the Ptolemy fault, (d) for coseismic uplift for the Cape Lithino faults, (e) for coseismic plus postseismic uplift (50% of the coseismic value for the Ptolemy fault, and, (f) for coseismic plus postseismic uplift (50% of the coseismic value for the Cape Lithino faults.

Figure 15:

3D cartoon of the study area illustrating that upper-plate extensional faults in the south central area of Crete may perturb regional uplift and have a controlling effect on the coastal topography. Differential uplift occurs along fault-length scales as a result of footwall and hangingwall deformation. Faults relevant to the study are labelled as: SCCF: South Central Crete Fault: Pt: Ptolemy fault; CL: Cape Lithino faults; Mr: Mirto fault

Figure 1.

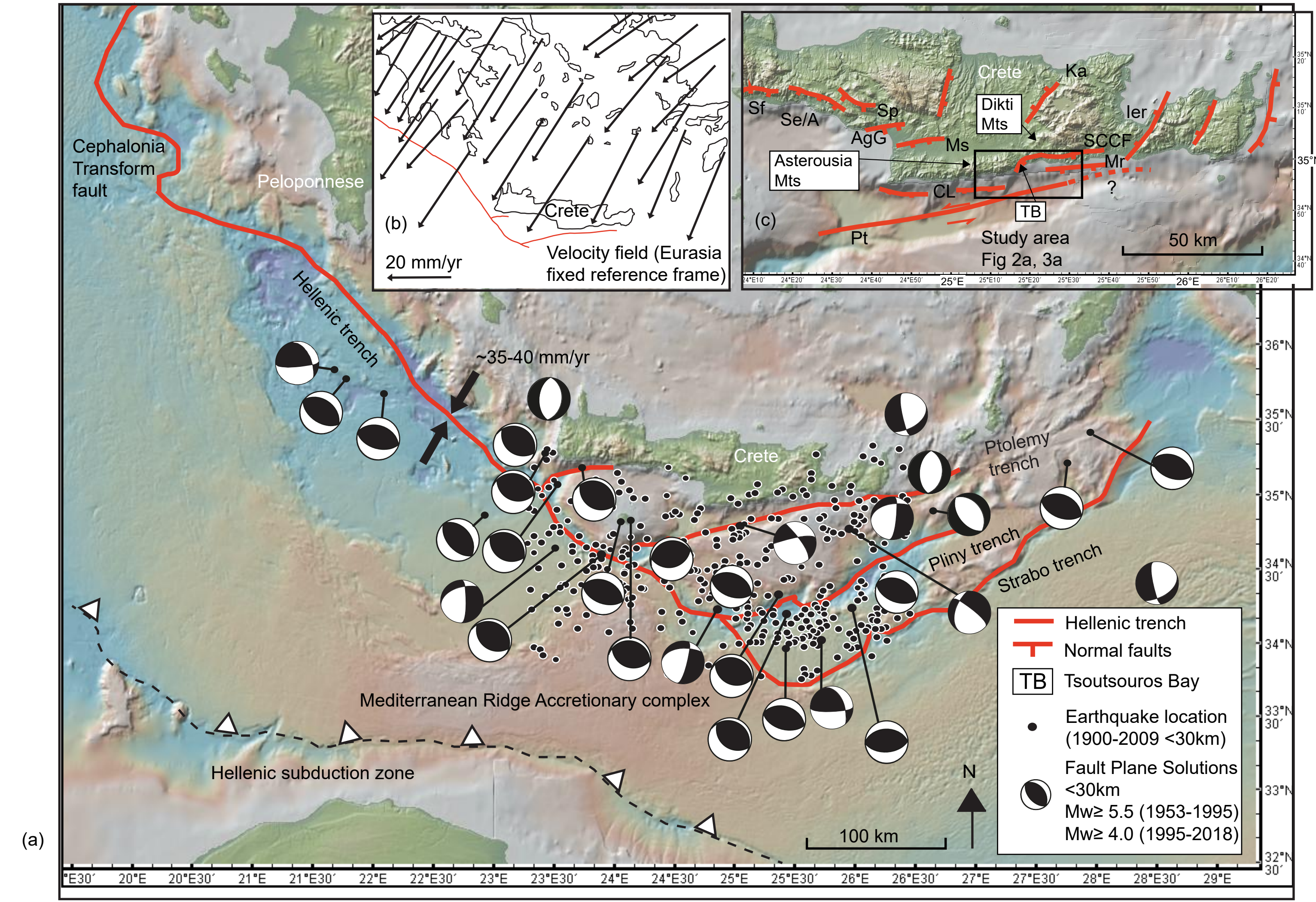

Cephalonia
Transform
fault
Peloponnese
Hellenic trench
~35-40 mm/yr
Crete
Ptolemy trench
Pliny trench
Strabo trench
Mediterranean Ridge Accretionary complex
Hellenic subduction zone
N
100 km
(b)
20 mm/yr
Crete
Velocity field (Eurasia fixed reference frame)
(c)
Crete
Ka
Dikti Mts
Sf
Se/A
Sp
AgG
Ms
Ier
SCCF
Mr
Asterousia Mts
CL
?
TB
Pt
Study area Fig 2a, 3a
50 km
Hellenic trench
Normal faults
TB Tsoutsouros Bay
Earthquake location (1900-2009 <30km)
Fault Plane Solutions <30km
Mw≥ 5.5 (1953-1995)
Mw≥ 4.0 (1995-2018)
(a)

Figure 2.

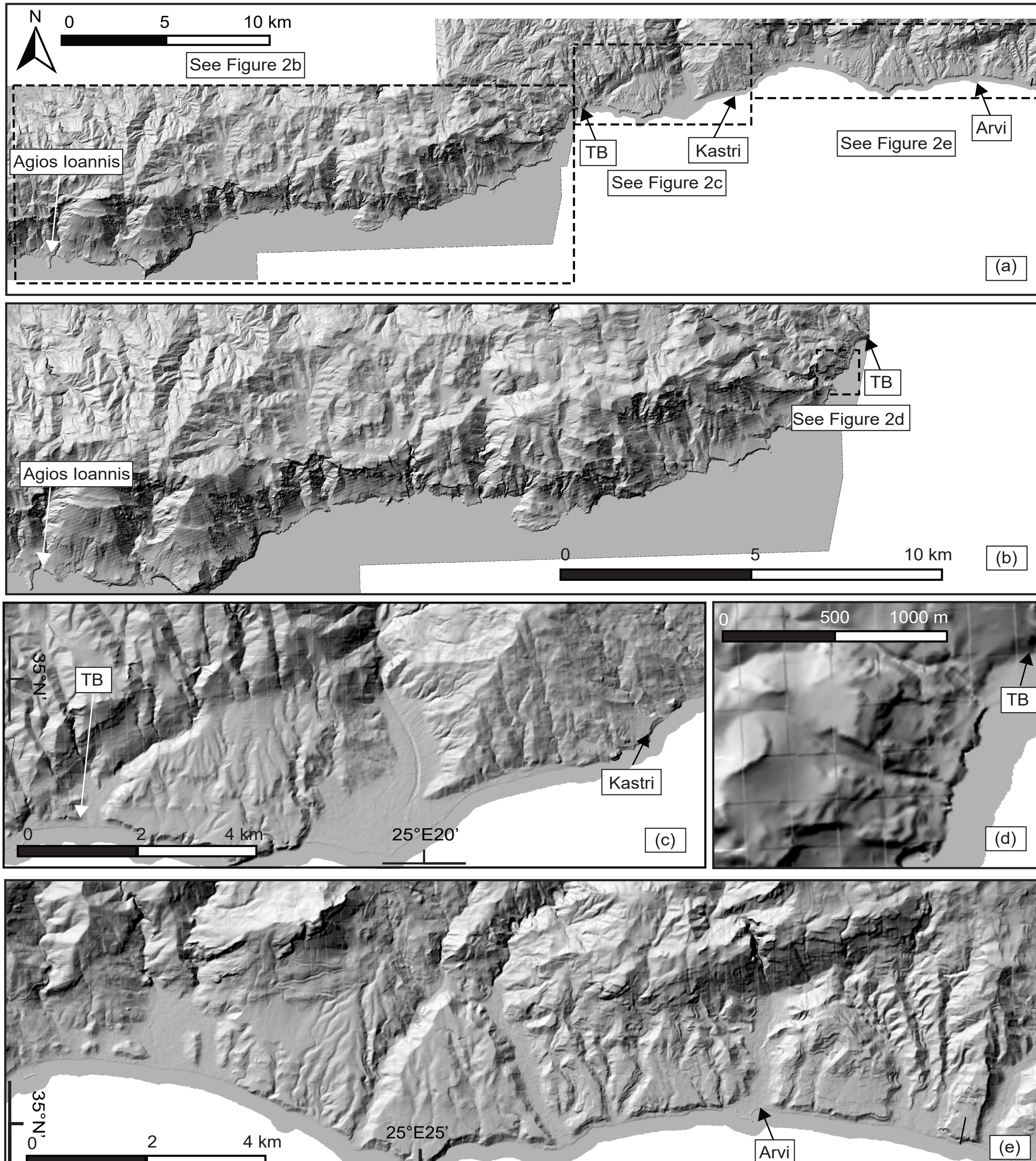

TB Tsoutsouros Bay

Arvi Local towns

Figure 3.

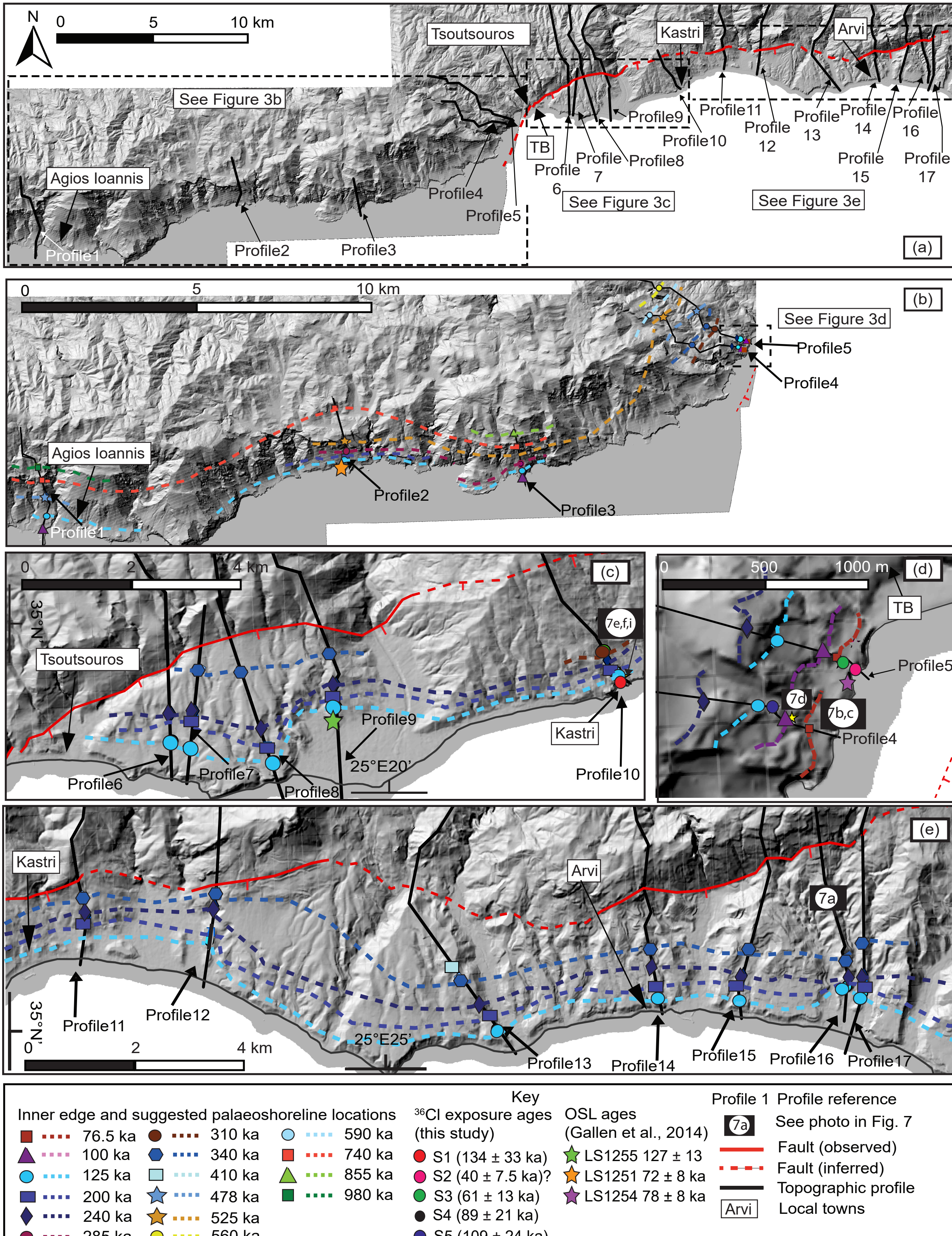

(a)
N
0 5 10 km
Tsoutsouros
Kastri
Arvi
See Figure 3b
See Figure 3c
See Figure 3e
Agios Ioannis
TB
Profile1
Profile2
Profile3
Profile4
Profile5
Profile 6
Profile 7
Profile8
Profile9
Profile10
Profile11
Profile 12
Profile 13
Profile 14
Profile 15
Profile 16
Profile 17
(b)
0 5 10 km
See Figure 3d
Agios Ioannis
Profile1
Profile2
Profile3
Profile4
Profile5
(c)
0 2 4 km
35°N'
Tsoutsouros
Kastri
7e,f,i
25°E20'
Profile6
Profile7
Profile8
Profile9
Profile10
(d)
0 500 1000 m
TB
7d
7b,c
Profile4
Profile5
(e)
Kastri
Arvi
7a
35°N'
25°E25'
0 2 4 km
Profile11
Profile12
Profile13
Profile14
Profile15
Profile16
Profile17
Key
Inner edge and suggested palaeoshoreline locations
76.5 ka
100 ka
125 ka
200 ka
240 ka
285 ka
310 ka
340 ka
410 ka
478 ka
525 ka
560 ka
590 ka
740 ka
855 ka
980 ka
36Cl exposure ages (this study)
S1 (134 ± 33 ka)
S2 (40 ± 7.5 ka)?
S3 (61 ± 13 ka)
S4 (89 ± 21 ka)
S5 (109 ± 24 ka)
OSL ages (Gallen et al., 2014)
LS1255 127 ± 13
LS1251 72 ± 8 ka
LS1254 78 ± 8 ka
Profile 1 Profile reference
7a See photo in Fig. 7
Fault (observed)
Fault (inferred)
Topographic profile
Arvi Local towns

Figure 4.

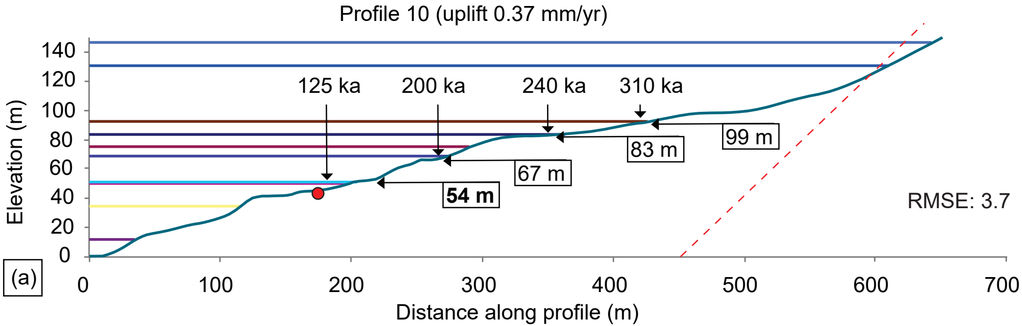

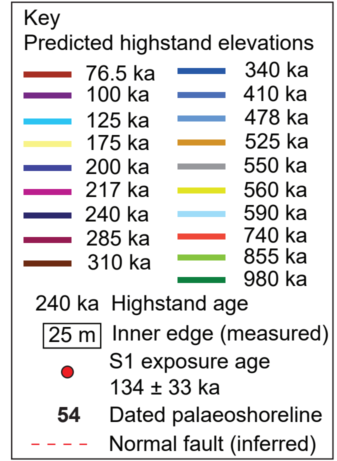

Uplift rate (mm/yr)	Highstand age (y), [relative sea level (m)]	Predicted elevation (m)	Measured elevation (m) *GPS **DEM
0.37	30000 [-80]	-69	
0.37	50000 [-60]	-42	
0.37	76500 [-30]	-2	
0.37	100000 [-25]	12	
0.37	125000 [5]	51	**54***
0.37	175000 [-30]	35	
0.37	200000 [-5]	69	67**
0.37	217000 [-30]	50	
0.37	240000 [-5]	84	83**
0.37	285000 [-30]	75	
0.37	310000 [-22]	93	99**
0.37	340000 [5]	131	
0.37	410000 [-5]	147	

(b)

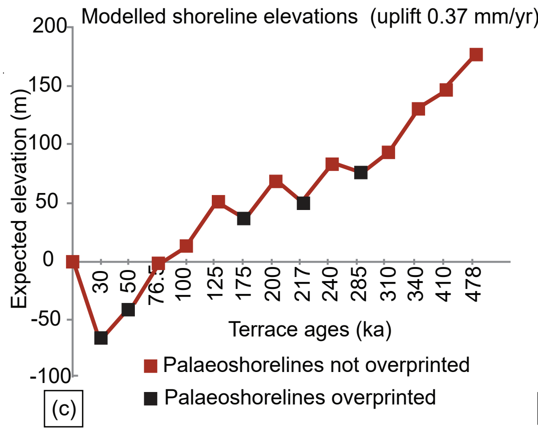

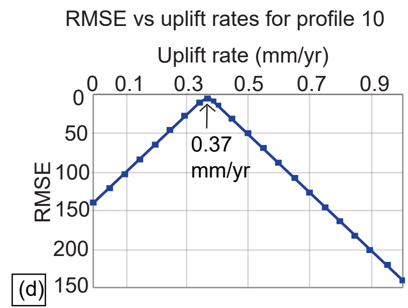

Figure 5.

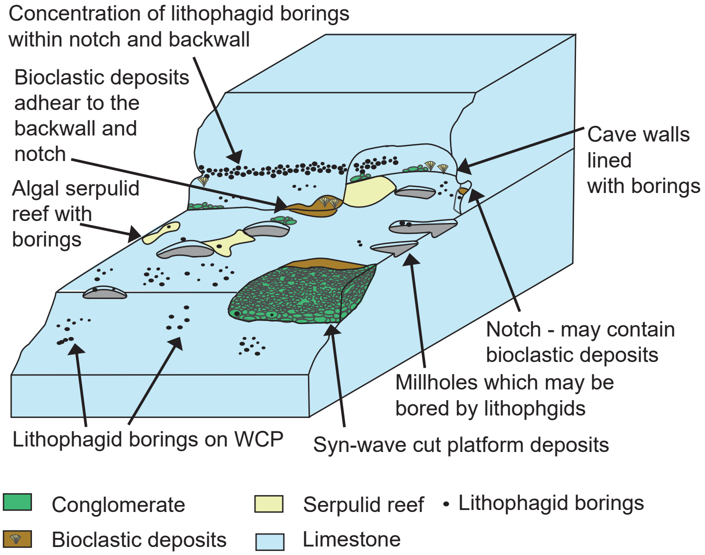
Concentration of lithophagid borings within notch and backwall
Bioclastic deposits adhear to the backwall and notch
Algal serpulid reef with borings
Cave walls lined with borings
Notch - may contain bioclastic deposits
Millholes which may be bored by lithophgids
Lithophagid borings on WCP
Syn-wave cut platform deposits
Conglomerate
Serpulid reef
• Lithophagid borings
Bioclastic deposits
Limestone

Figure 6.

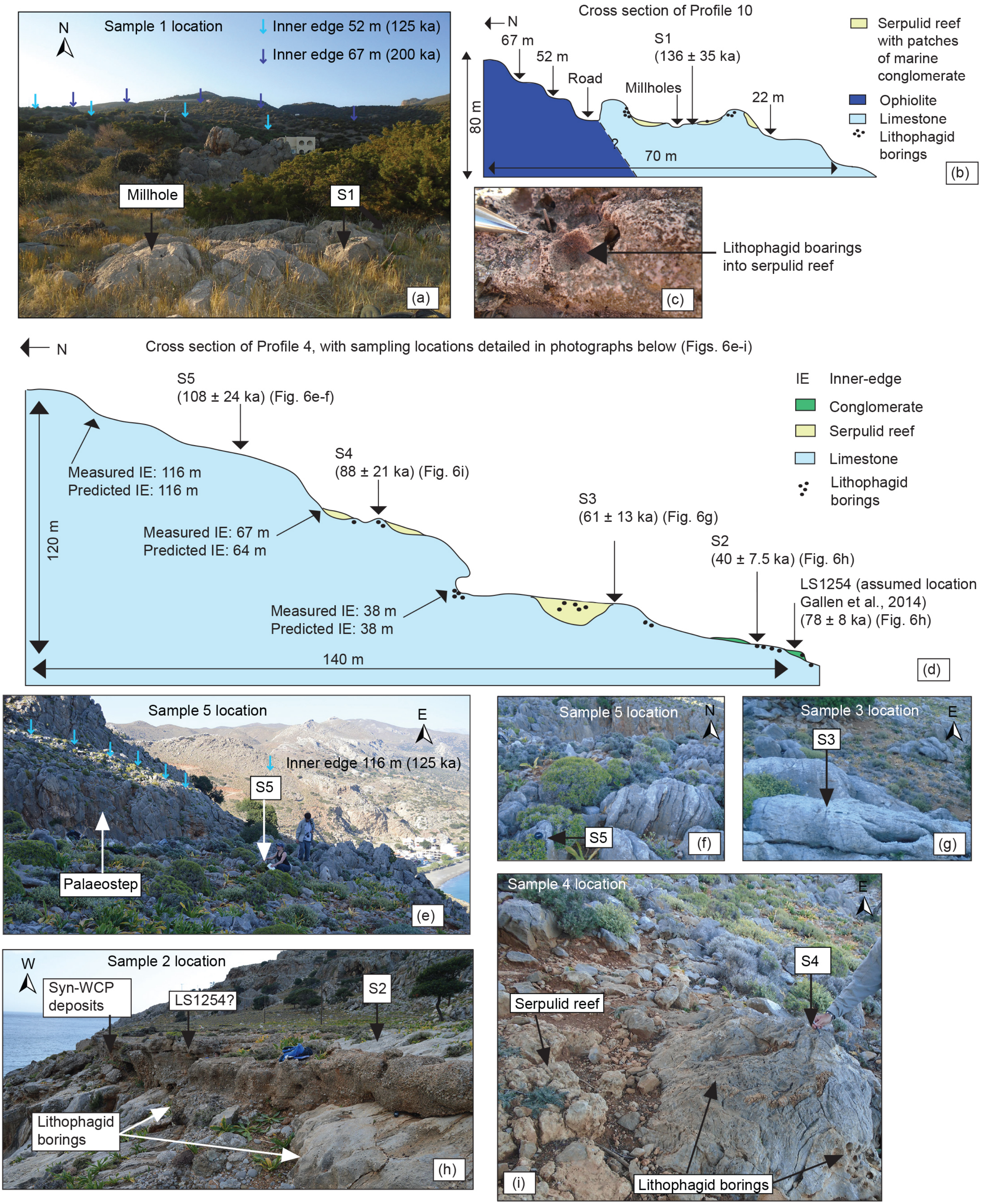

Sample 1 location
N
Inner edge 52 m (125 ka)
Inner edge 67 m (200 ka)
Millhole
S1
(a)
Cross section of Profile 10
N
67 m
52 m
Road
S1
(136 ± 35 ka)
Millholes
22 m
80 m
70 m
Serpulid reef with patches of marine conglomerate
Ophiolite
Limestone
Lithophagid borings
(b)
Lithophagid boarings into serpulid reef
(c)
N
Cross section of Profile 4, with sampling locations detailed in photographs below (Figs. 6e-i)
S5
(108 ± 24 ka) (Fig. 6e-f)
Measured IE: 116 m
Predicted IE: 116 m
S4
(88 ± 21 ka) (Fig. 6i)
Measured IE: 67 m
Predicted IE: 64 m
S3
(61 ± 13 ka) (Fig. 6g)
Measured IE: 38 m
Predicted IE: 38 m
S2
(40 ± 7.5 ka) (Fig. 6h)
LS1254 (assumed location Gallen et al., 2014)
(78 ± 8 ka) (Fig. 6h)
120 m
140 m
IE Inner-edge
Conglomerate
Serpulid reef
Limestone
Lithophagid borings
(d)
Sample 5 location
E
Inner edge 116 m (125 ka)
S5
Palaeostep
(e)
Sample 5 location
N
S5
(f)
Sample 3 location
E
S3
(g)
Sample 2 location
W
Syn-WCP deposits
LS1254?
S2
Lithophagid borings
(h)
Sample 4 location
E
S4
Serpulid reef
Lithophagid borings
(i)

Figure 7.

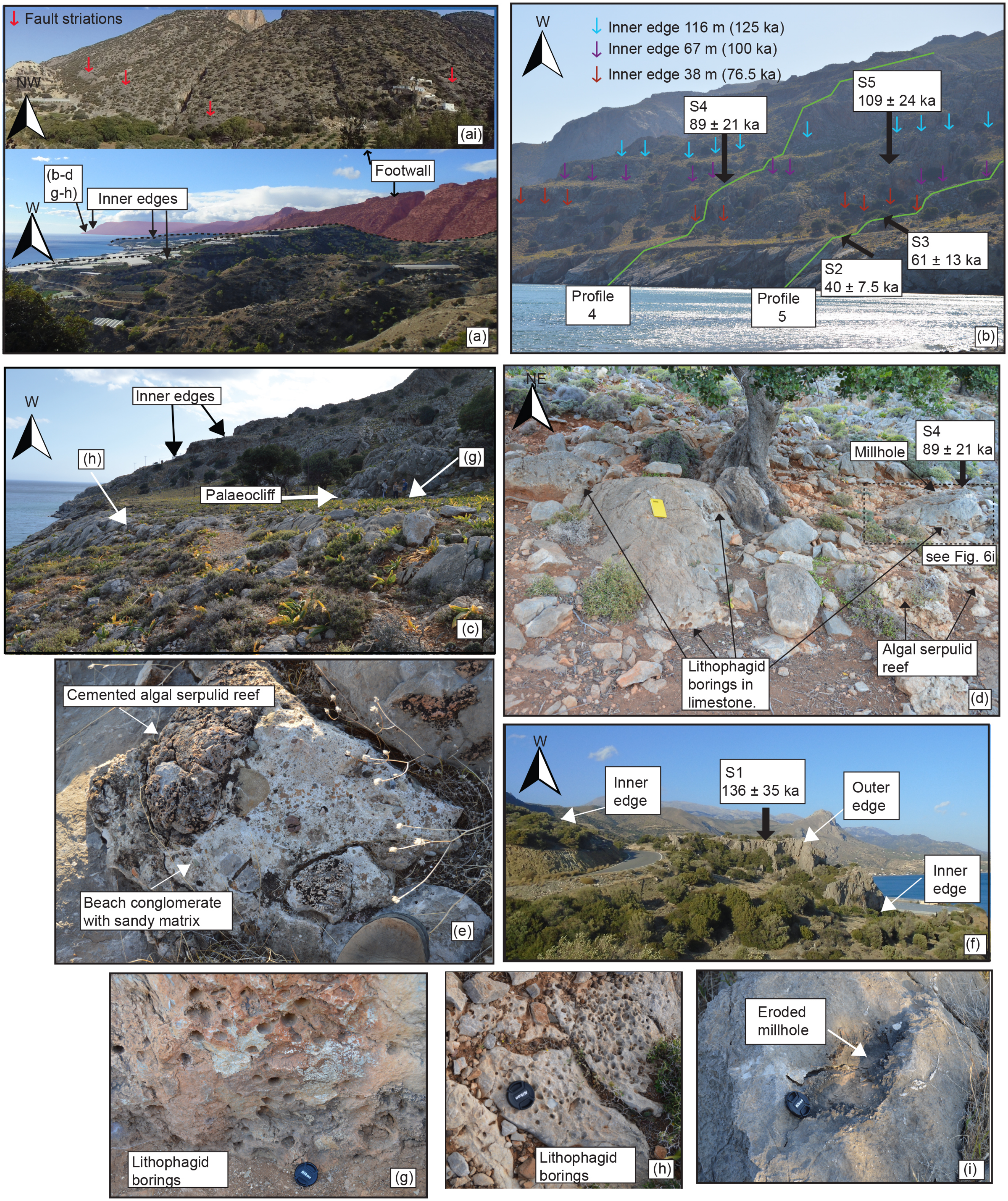

Fault striations
NW
(ai)
Footwall
(b-d g-h)
Inner edges
W
(a)
W
Inner edge 116 m (125 ka)
Inner edge 67 m (100 ka)
Inner edge 38 m (76.5 ka)
S4
89 ± 21 ka
S5
109 ± 24 ka
S3
61 ± 13 ka
S2
40 ± 7.5 ka
Profile 4
Profile 5
(b)
W
Inner edges
(h)
(g)
Palaeocliff
(c)
NE
S4
89 ± 21 ka
Millhole
see Fig. 6i
Lithophagid borings in limestone.
Algal serpulid reef
(d)
Cemented algal serpulid reef
Beach conglomerate with sandy matrix
(e)
W
Inner edge
S1
136 ± 35 ka
Outer edge
Inner edge
(f)
Lithophagid borings
(g)
Lithophagid borings
(h)
Eroded millhole
(i)

Figure 8.

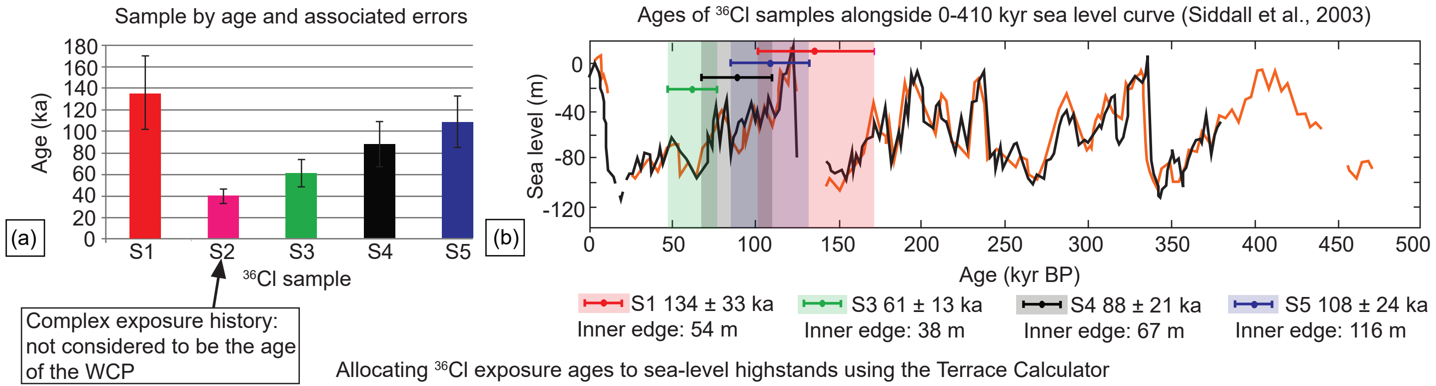

Allocating ^{36}Cl exposure ages to sea-level highstands using the Terrace Calculator

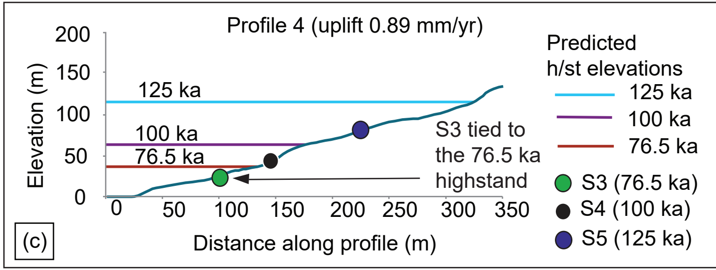

Uplift (mm/yr)	Highstands (ka)	Highstand elevations (m)		R^2 (Predicted vs measured)*
		Predicted (Terrace Calc)	Measured (Field/DEM)	
0.89	76.5	38	38	0.9991
	100	64	67	
	125	116	116	

(see Supplementary Figure 1 for all tested uplift options)

* R^2 values are for all measured palaeoshoreline values compared to predicted values (to 980 ka)

Figure 9.

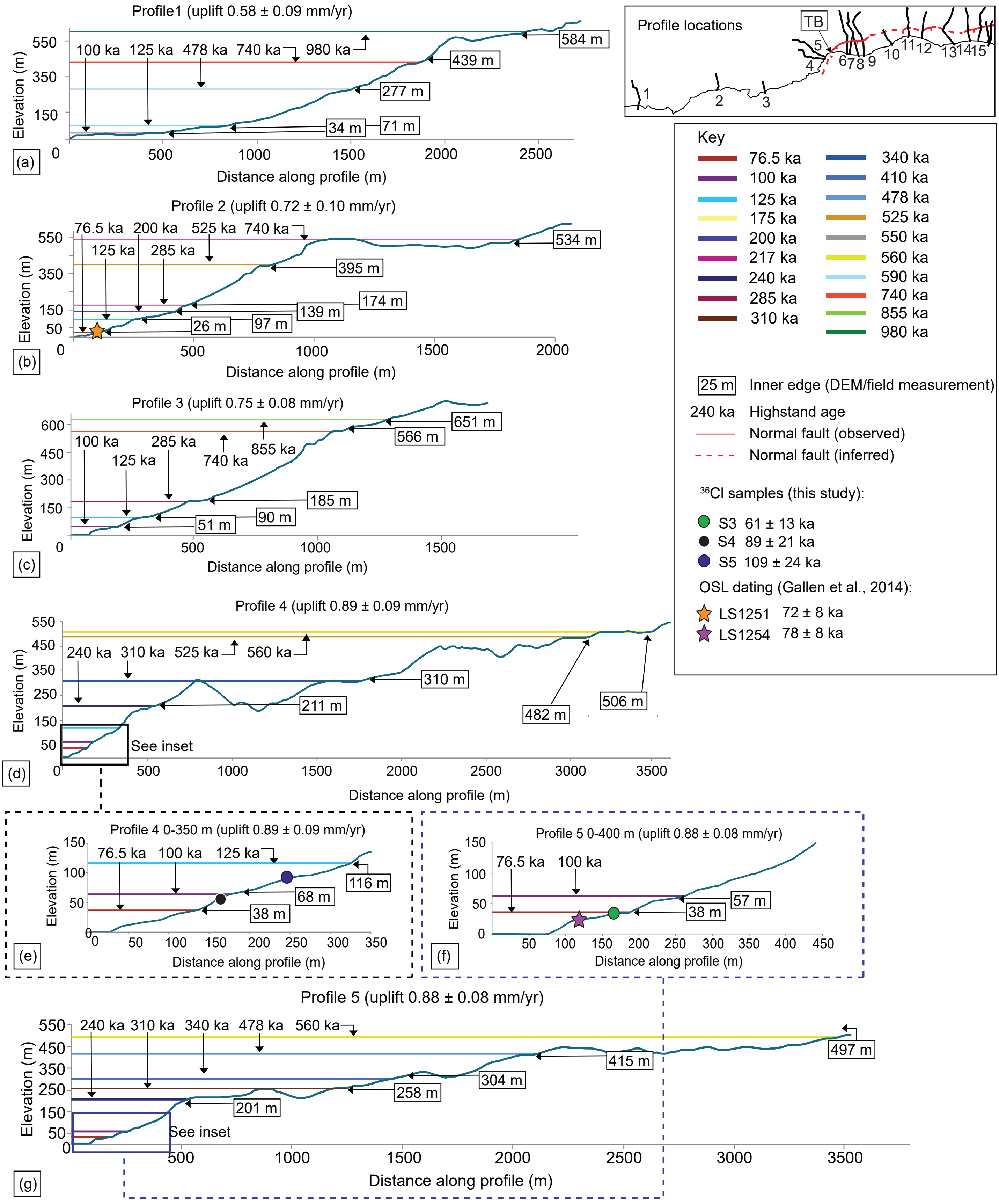

Profile1 (uplift 0.58 ± 0.09 mm/yr)
(a)
Elevation (m)
Distance along profile (m)
100 ka 125 ka 478 ka 740 ka 980 ka
584 m
439 m
277 m
34 m
71 m
Profile locations
TB
Key
76.5 ka
100 ka
125 ka
175 ka
200 ka
217 ka
240 ka
285 ka
310 ka
340 ka
410 ka
478 ka
525 ka
550 ka
560 ka
590 ka
740 ka
855 ka
980 ka
25 m Inner edge (DEM/field measurement)
240 ka Highstand age
Normal fault (observed)
Normal fault (inferred)
36Cl samples (this study):
S3 61 ± 13 ka
S4 89 ± 21 ka
S5 109 ± 24 ka
OSL dating (Gallen et al., 2014):
LS1251 72 ± 8 ka
LS1254 78 ± 8 ka
Profile 2 (uplift 0.72 ± 0.10 mm/yr)
(b)
76.5 ka 200 ka 525 ka 740 ka
125 ka 285 ka
534 m
395 m
174 m
139 m
26 m
97 m
Profile 3 (uplift 0.75 ± 0.08 mm/yr)
(c)
100 ka 285 ka
125 ka 740 ka 855 ka
651 m
566 m
185 m
90 m
51 m
Profile 4 (uplift 0.89 ± 0.09 mm/yr)
(d)
240 ka 310 ka 525 ka 560 ka
310 m
211 m
482 m
506 m
See inset
Profile 4 0-350 m (uplift 0.89 ± 0.09 mm/yr)
(e)
76.5 ka 100 ka 125 ka
116 m
68 m
38 m
Profile 5 0-400 m (uplift 0.88 ± 0.08 mm/yr)
(f)
76.5 ka 100 ka
57 m
38 m
Profile 5 (uplift 0.88 ± 0.08 mm/yr)
(g)
240 ka 310 ka 340 ka 478 ka 560 ka
497 m
415 m
304 m
258 m
201 m
See inset

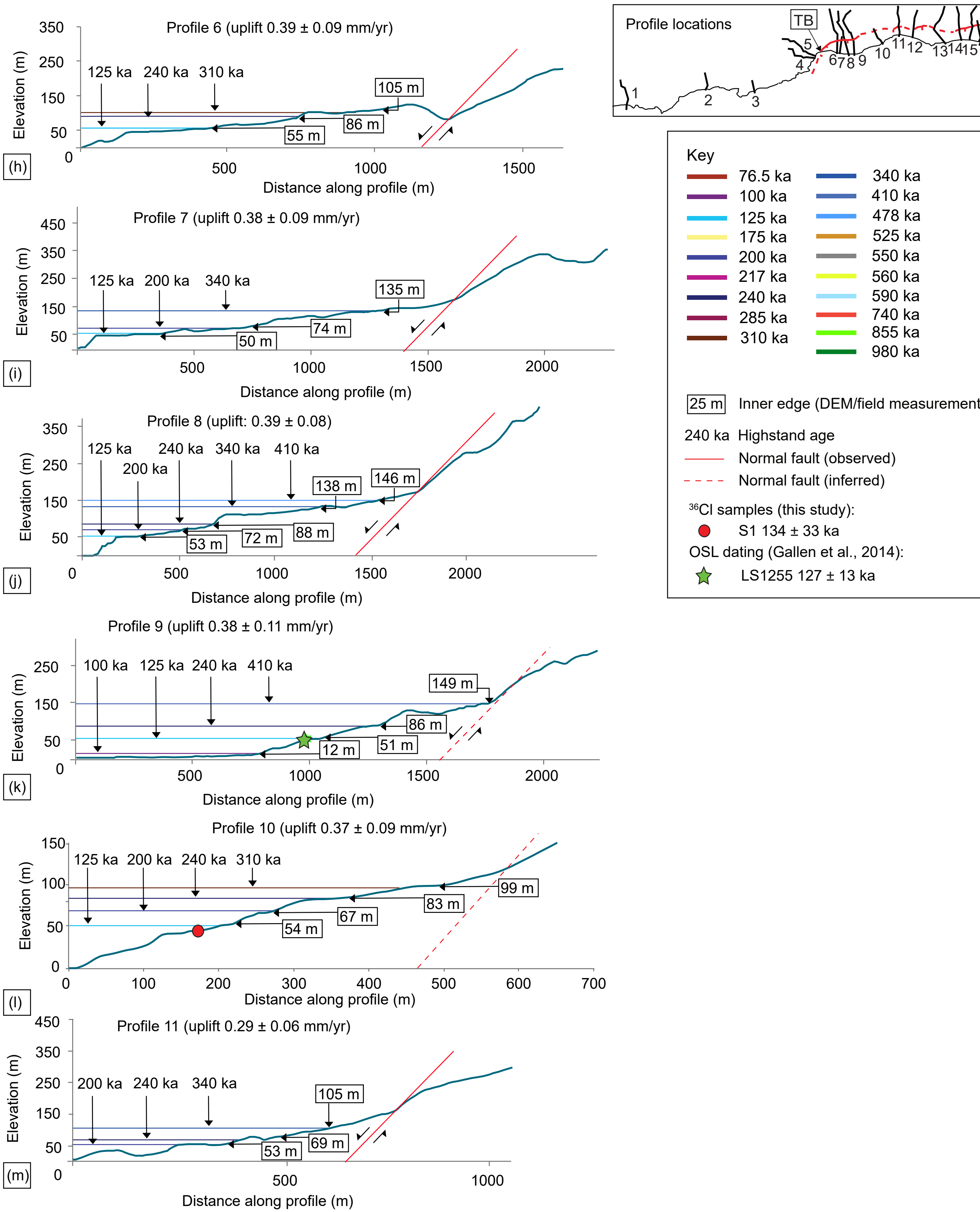

Profile 6 (uplift 0.39 ± 0.09 mm/yr)
Elevation (m)
350
250
150
50
0
125 ka
240 ka
310 ka
105 m
86 m
55 m
500
1000
1500
Distance along profile (m)
(h)
Profile 7 (uplift 0.38 ± 0.09 mm/yr)
450
350
250
150
50
125 ka
200 ka
340 ka
135 m
74 m
50 m
500
1000
1500
2000
(i)
Profile 8 (uplift: 0.39 ± 0.08)
125 ka
200 ka
240 ka
340 ka
410 ka
138 m
146 m
88 m
72 m
53 m
(j)
Profile 9 (uplift 0.38 ± 0.11 mm/yr)
100 ka
125 ka
240 ka
410 ka
149 m
86 m
51 m
12 m
(k)
Profile 10 (uplift 0.37 ± 0.09 mm/yr)
150
100
125 ka
200 ka
240 ka
310 ka
99 m
83 m
67 m
54 m
0
100
200
300
400
500
600
700
(l)
Profile 11 (uplift 0.29 ± 0.06 mm/yr)
200 ka
240 ka
340 ka
105 m
69 m
53 m
(m)
Profile locations
TB
1
2
3
4
5
6
7
8
9
10
11
12
13
14
15
Key
76.5 ka
100 ka
125 ka
175 ka
200 ka
217 ka
240 ka
285 ka
310 ka
340 ka
410 ka
478 ka
525 ka
550 ka
560 ka
590 ka
740 ka
855 ka
980 ka
25 m
Inner edge (DEM/field measurement)
240 ka
Highstand age
Normal fault (observed)
Normal fault (inferred)
36Cl samples (this study):
S1 134 ± 33 ka
OSL dating (Gallen et al., 2014):
LS1255 127 ± 13 ka

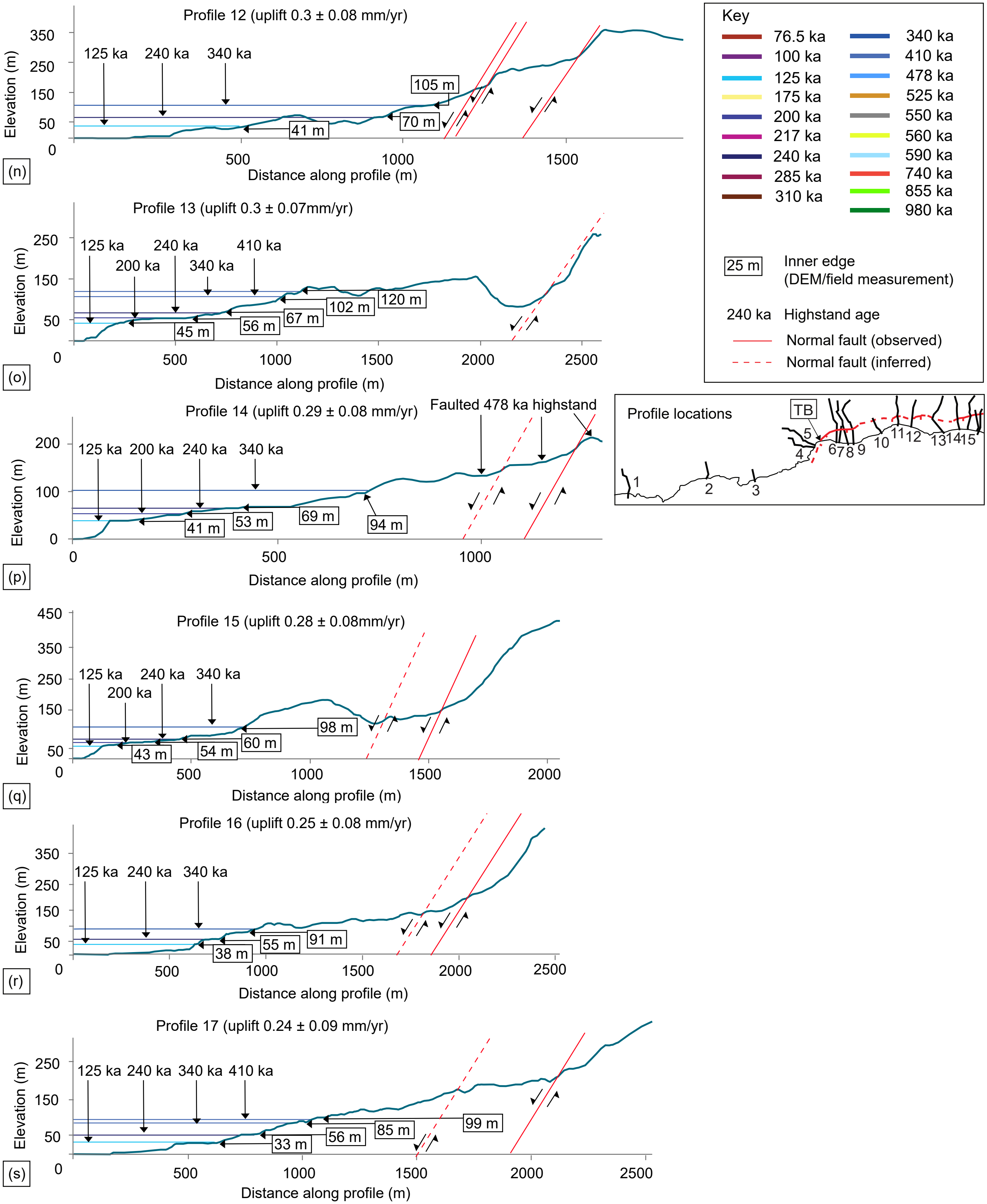

Profile 12 (uplift 0.3 ± 0.08 mm/yr)
Elevation (m)
Distance along profile (m)
125 ka
240 ka
340 ka
105 m
70 m
41 m
(n)
Profile 13 (uplift 0.3 ± 0.07mm/yr)
125 ka
200 ka
240 ka
340 ka
410 ka
45 m
56 m
67 m
102 m
120 m
(o)
Profile 14 (uplift 0.29 ± 0.08 mm/yr)
Faulted 478 ka highstand
125 ka
200 ka
240 ka
340 ka
41 m
53 m
69 m
94 m
(p)
Profile 15 (uplift 0.28 ± 0.08mm/yr)
125 ka
200 ka
240 ka
340 ka
43 m
54 m
60 m
98 m
(q)
Profile 16 (uplift 0.25 ± 0.08 mm/yr)
125 ka
240 ka
340 ka
38 m
55 m
91 m
(r)
Profile 17 (uplift 0.24 ± 0.09 mm/yr)
125 ka
240 ka
340 ka
410 ka
33 m
56 m
85 m
99 m
(s)
Key
76.5 ka
100 ka
125 ka
175 ka
200 ka
217 ka
240 ka
285 ka
310 ka
340 ka
410 ka
478 ka
525 ka
550 ka
560 ka
590 ka
740 ka
855 ka
980 ka
25 m
Inner edge (DEM/field measurement)
240 ka
Highstand age
Normal fault (observed)
Normal fault (inferred)
Profile locations
TB
1
2
3
4
5
6
7
8
9
10
11
12
13
14
15

Figure 10.

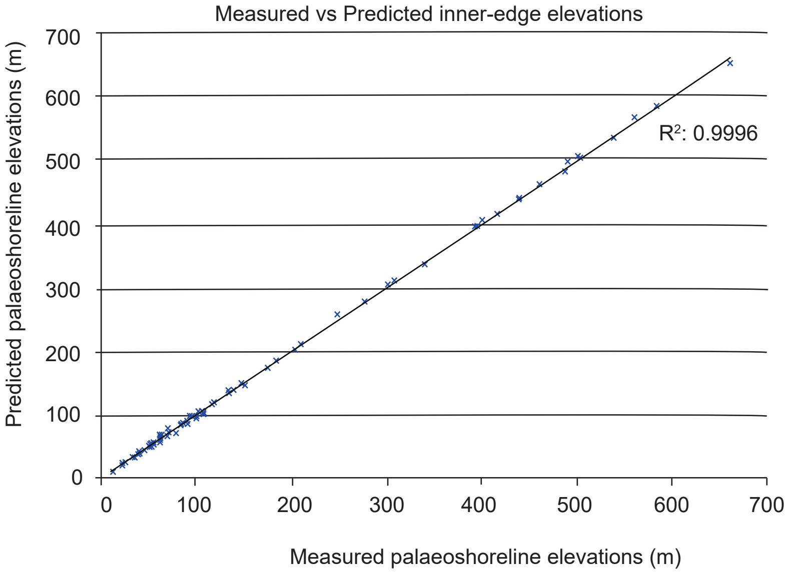
Measured vs Predicted inner-edge elevations
Predicted palaeoshoreline elevations (m)
Measured palaeoshoreline elevations (m)
R^2: 0.9996
0
100
200
300
400
500
600
700

Figure 11.

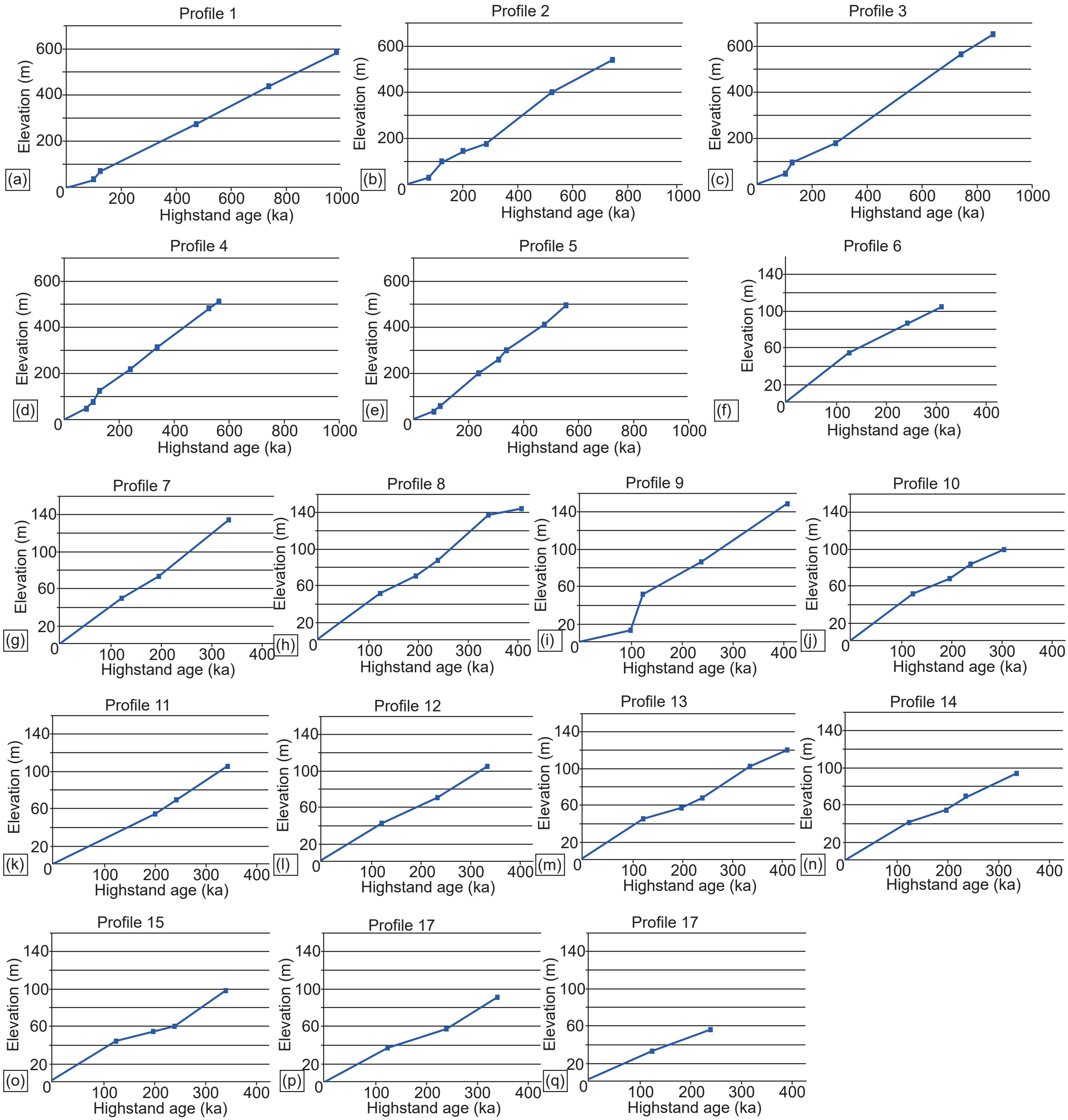

Profile 1
Profile 2
Profile 3
Profile 4
Profile 5
Profile 6
Profile 7
Profile 8
Profile 9
Profile 10
Profile 11
Profile 12
Profile 13
Profile 14
Profile 15
Profile 17
Profile 17
(a)
(b)
(c)
(d)
(e)
(f)
(g)
(h)
(i)
(j)
(k)
(l)
(m)
(n)
(o)
(p)
(q)
Elevation (m)
Highstand age (ka)

Figure 12.

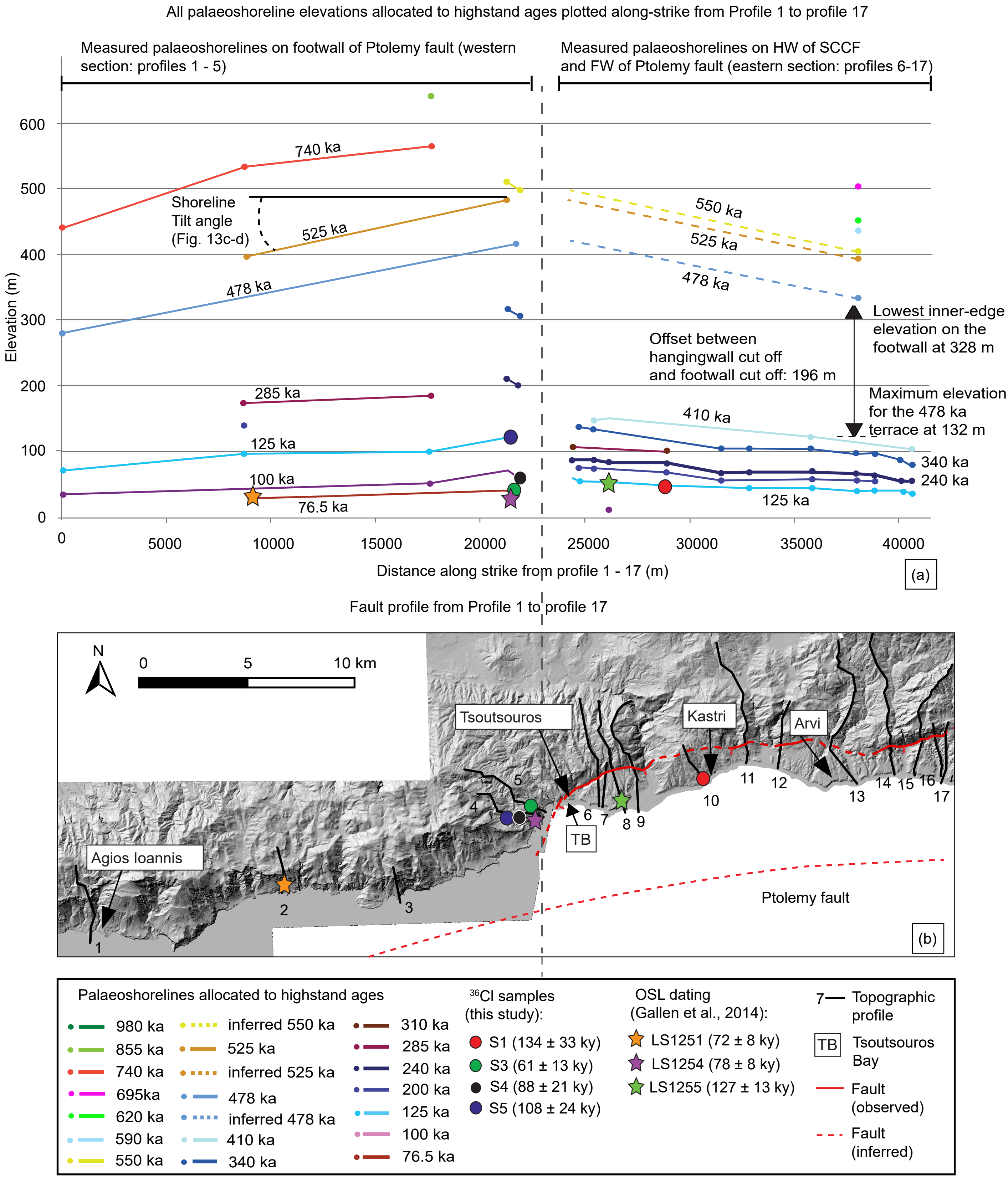
All palaeoshoreline elevations allocated to highstand ages plotted along-strike from Profile 1 to profile 17
Measured palaeoshorelines on footwall of Ptolemy fault (western section: profiles 1 - 5)
Measured palaeoshorelines on HW of SCCF and FW of Ptolemy fault (eastern section: profiles 6-17)
Elevation (m)
600
500
400
300
200
100
0
740 ka
Shoreline Tilt angle (Fig. 13c-d)
525 ka
478 ka
285 ka
125 ka
100 ka
76.5 ka
550 ka
525 ka
478 ka
Lowest inner-edge elevation on the footwall at 328 m
Offset between hangingwall cut off and footwall cut off: 196 m
Maximum elevation for the 478 ka terrace at 132 m
410 ka
340 ka
240 ka
125 ka
0
5000
10000
15000
20000
25000
30000
35000
40000
Distance along strike from profile 1 - 17 (m)
(a)
Fault profile from Profile 1 to profile 17
N
0
5
10 km
Tsoutsouros
Kastri
Arvi
Agios Ioannis
TB
Ptolemy fault
1
2
3
4
5
6
7
8
9
10
11
12
13
14
15
16
17
(b)
Palaeoshorelines allocated to highstand ages
980 ka
855 ka
740 ka
695ka
620 ka
590 ka
550 ka
inferred 550 ka
525 ka
inferred 525 ka
478 ka
inferred 478 ka
410 ka
340 ka
310 ka
285 ka
240 ka
200 ka
125 ka
100 ka
76.5 ka
36Cl samples (this study):
S1 (134 ± 33 ky)
S3 (61 ± 13 ky)
S4 (88 ± 21 ky)
S5 (108 ± 24 ky)
OSL dating (Gallen et al., 2014):
LS1251 (72 ± 8 ky)
LS1254 (78 ± 8 ky)
LS1255 (127 ± 13 ky)
7 Topographic profile
TB Tsoutsouros Bay
Fault (observed)
Fault (inferred)

Figure 13.

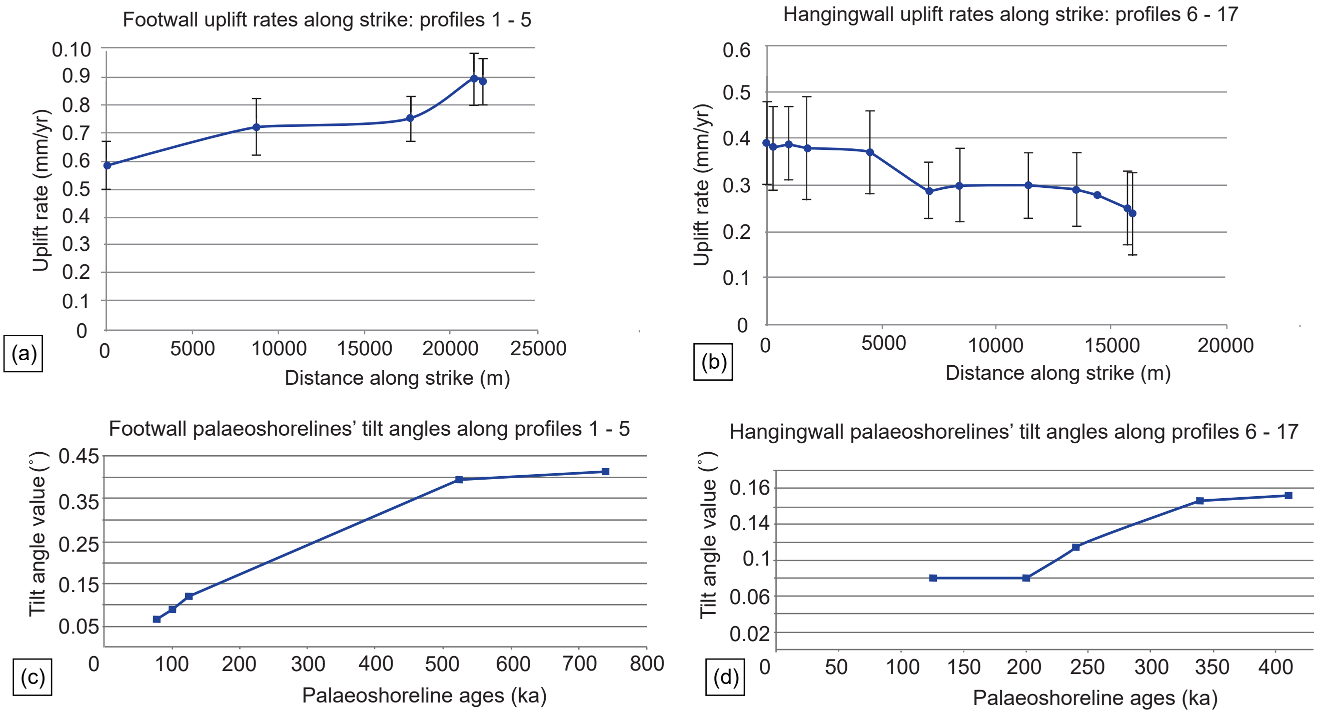
Footwall uplift rates along strike: profiles 1 - 5
Uplift rate (mm/yr)
0.10
0.9
0.8
0.7
0.6
0.5
0.4
0.3
0.2
0.1
0
0
5000
10000
15000
20000
25000
Distance along strike (m)
(a)
Hangingwall uplift rates along strike: profiles 6 - 17
Uplift rate (mm/yr)
0.6
0.5
0.4
0.3
0.2
0.1
0
0
5000
10000
15000
20000
Distance along strike (m)
(b)
Footwall palaeoshorelines' tilt angles along profiles 1 - 5
Tilt angle value (°)
0.45
0.35
0.25
0.15
0.05
0
100
200
300
400
500
600
700
800
Palaeoshoreline ages (ka)
(c)
Hangingwall palaeoshorelines' tilt angles along profiles 6 - 17
Tilt angle value (°)
0.16
0.14
0.1
0.06
0.02
0
50
100
150
200
250
300
350
400
Palaeoshoreline ages (ka)
(d)

Figure 14.

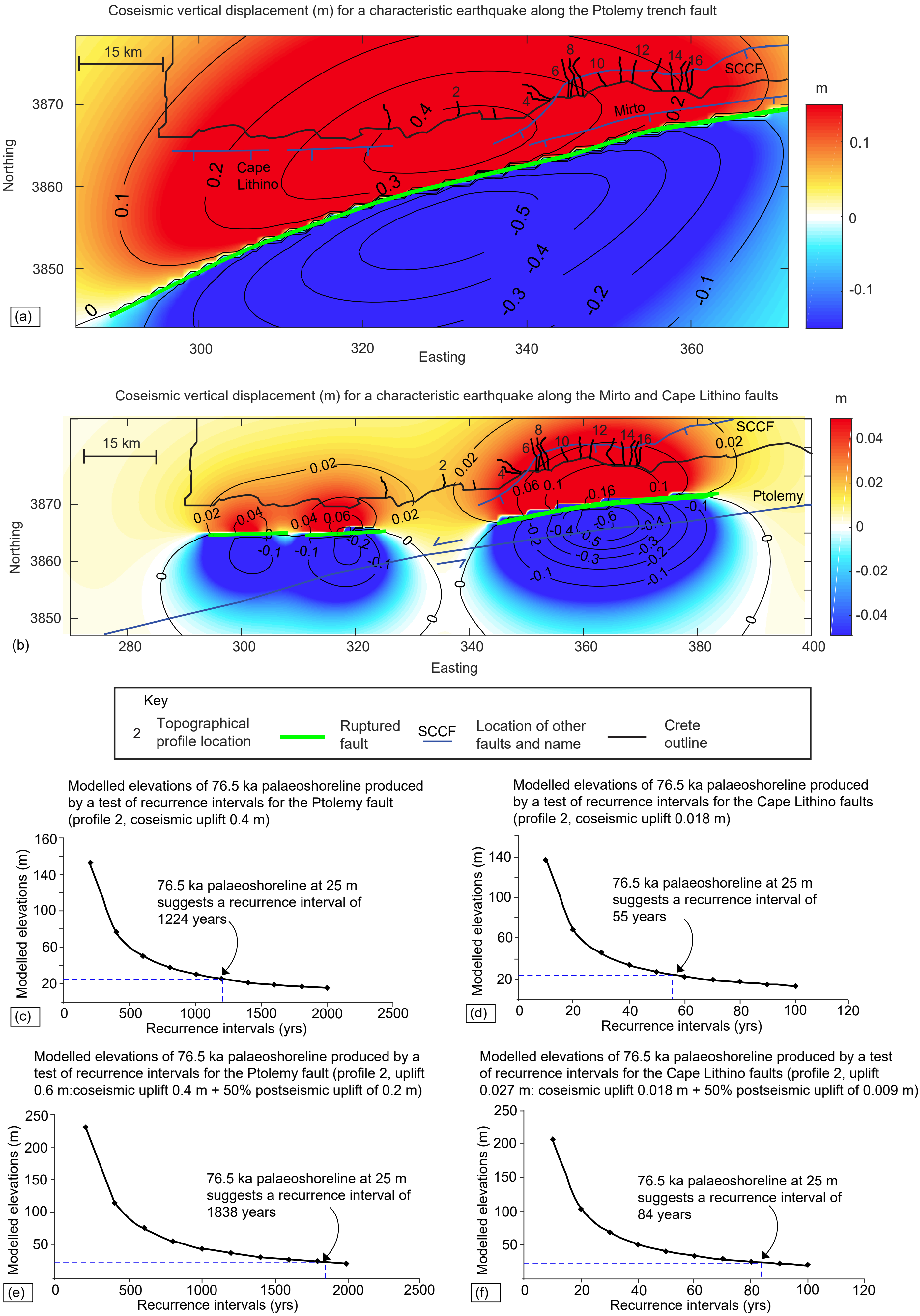

Coseismic vertical displacement (m) for a characteristic earthquake along the Ptolemy trench fault
15 km
Cape Lithino
Mirto
SCCF
Northing
Easting
m
(a)
Coseismic vertical displacement (m) for a characteristic earthquake along the Mirto and Cape Lithino faults
15 km
SCCF
Ptolemy
Northing
Easting
m
(b)
Key
2 Topographical profile location
Ruptured fault
SCCF Location of other faults and name
Crete outline
Modelled elevations of 76.5 ka palaeoshoreline produced by a test of recurrence intervals for the Ptolemy fault (profile 2, coseismic uplift 0.4 m)
76.5 ka palaeoshoreline at 25 m suggests a recurrence interval of 1224 years
Modelled elevations (m)
Recurrence intervals (yrs)
(c)
Modelled elevations of 76.5 ka palaeoshoreline produced by a test of recurrence intervals for the Cape Lithino faults (profile 2, coseismic uplift 0.018 m)
76.5 ka palaeoshoreline at 25 m suggests a recurrence interval of 55 years
Modelled elevations (m)
Recurrence intervals (yrs)
(d)
Modelled elevations of 76.5 ka palaeoshoreline produced by a test of recurrence intervals for the Ptolemy fault (profile 2, uplift 0.6 m:coseismic uplift 0.4 m + 50% postseismic uplift of 0.2 m)
76.5 ka palaeoshoreline at 25 m suggests a recurrence interval of 1838 years
Modelled elevations (m)
Recurrence intervals (yrs)
(e)
Modelled elevations of 76.5 ka palaeoshoreline produced by a test of recurrence intervals for the Cape Lithino faults (profile 2, uplift 0.027 m: coseismic uplift 0.018 m + 50% postseismic uplift of 0.009 m)
76.5 ka palaeoshoreline at 25 m suggests a recurrence interval of 84 years
Modelled elevations (m)
Recurrence intervals (yrs)
(f)

Figure 15.

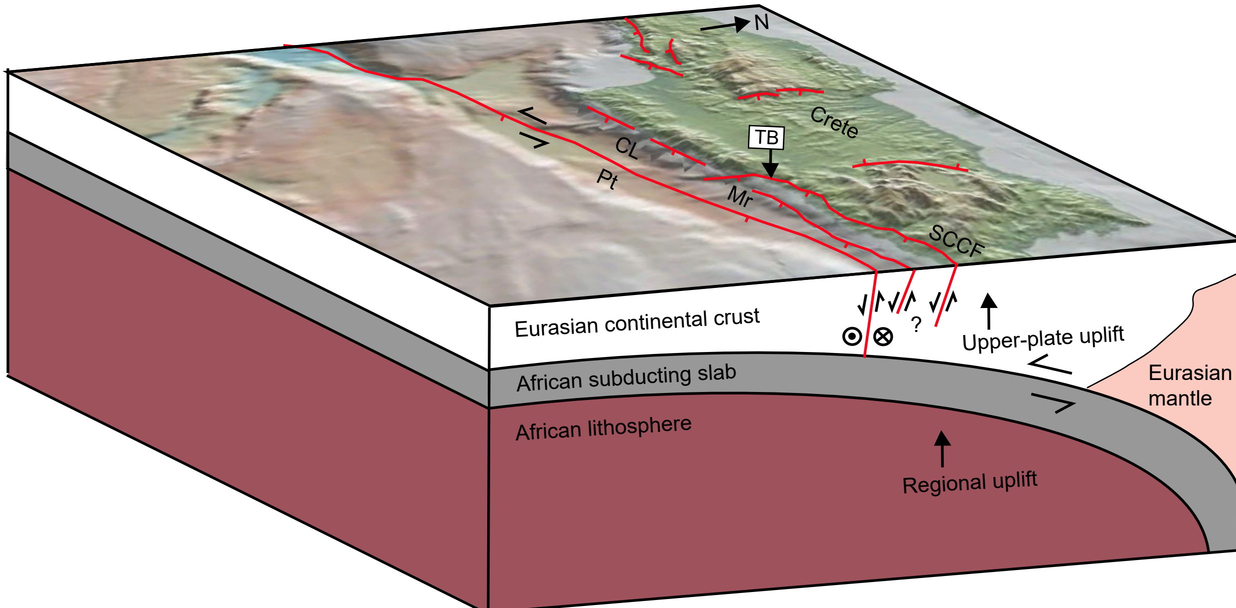
N
Crete
TB
CL
Pt
Mr
SCCF
?
Eurasian continental crust
Upper-plate uplift
African subducting slab
Eurasian mantle
African lithosphere
Regional uplift